1-29-2009

Synthesis and characterization of cerium-doped lanthanum halide colloidal nanocrystals

Krishnaprasad Sankar

Krishnaprasad Sankar

Candidate

Electrical and Computer Engineering

Department

This thesis is approved, and it is acceptable in quality and form for publication on microfilm:

Approved by the Thesis Committee:

Dr. Marek Osiński

Dr. Sanjay Krishna

Dr. Ganesh Balakrishnan

Accepted:

Dean, Graduate School

Date

SYNTHESIS AND CHARACTERIZATION OF CERIUM-DOPED LANTHANUM HALIDE COLLOIDAL NANOCRYSTALS

By

Krishnaprasad Sankar

B.E., Electrical and Electronics Engineering, Anna University, 2006

THESIS

Submitted in Partial Fulfillment of the
Requirements for the Degree of

Master of Science
Electrical Engineering

The University of New Mexico
Albuquerque, New Mexico

December, 2008

Dedication

To my parents Mrs. Nirmala Sankar and Mr. Sankar Narayanan

for their love and support throughout my life

To my teachers in school and college

I am what I am today because of them

To my dear friend Tosifa A. Memon

To god

ACKNOWLEDGEMENT

I would like to thank Dr. Marek Osiński, my advisor and thesis chair, for his guidance, support, encouragement during my Master's program, and also for being an outstanding research guide.

I am grateful to Dr. Sanjay Krishna, and Dr. Ganesh Balakrishnan for accepting to be my thesis committee members. I would like to thank them for their time.

I take this opportunity to acknowledge Mr. Chandrashekaran, my 10^{th} grade science teacher, and Mr. David, my 12^{th} grade physics teacher for instilling in me the interest in science and research.

I would like to thank my brother, Easwar Prasad Sankar for encouraging me to pursue Master's at UNM and for providing continuous guidance during the last two years.

Finally, I convey many heartfelt thanks to all my friends here in Albuquerque for their love and support and for making my two years here exceptionally enjoyable.

SYNTHESIS AND CHARACTERIZATION OF CERIUM-DOPED LANTHANUM HALIDE COLLOIDAL NANOCRYSTALS

By

Krishnaprasad Sankar

ABSTRACT OF THESIS

Submitted in Partial Fulfillment of the
Requirements for the Degree of

Master of Science
Electrical Engineering

The University of New Mexico
Albuquerque, New Mexico

December, 2008

SYNTHESIS AND CHARACTERIZATION OF CERIUM-DOPED LANTHANUM HALIDE COLLOIDAL NANOCRYSTALS

By

Krishnaprasad Sankar

B.E. Electrical and Electronics Engineering, Anna University, 2006
M.S. Electrical Engineering, University of New Mexico, 2008

ABSTRACT

Cerium-doped bulk lanthanum halide compounds are attractive in the field of high-energy radiation detection due to their interesting properties that include efficient radiation absorption, highly luminescent activator (cerium) emission through atomic transitions, host lattice protecting activators to prevent luminescence quenching, and fast decay-time radiative transitions between cerium levels. Cerium-doped bulk lanthanum bromide is reported to have a light yield of 60,000 photons/MeV, 2.5% full-width-to-half-maximum energy resolution (variation in emission light yield to absorbed gamma energy) for 662 keV gamma rays, 25 ns short decay time, and a density of 5.3 g/cm^3 with 22 mm attenuation length for 511 keV gamma rays. However, the crystals are hygroscopic and hence have to be protected from external environment both during growth and use.

Deriving the motivation from this material, this work strives at successful synthesis of stable cerium-doped lanthanum bromide/undoped lanthanum fluoride core/shell nanocrystals through inexpensive and repeatable colloidal routes. Following a systematic approach, cerium-doped lanthanum fluoride colloidal nanocrystals were synthesized through water-based and water-free (anhydrous) routes. Furthermore, core/shell synthesis of cerium-doped lanthanum fluoride/undoped lanthanum fluoride nanocrystals was achieved through the anhydrous route.

The optimum cerium concentration (x) was empirically identified in the $Ce_xLa_{1-x}F_3$ nanocrystal system in terms of light output from the activator levels of cerium. The persistence to high energy ionizing radiation was tested with a monoenergetic ^{137}Cs gamma source. Cerium-doped lanthanum fluoride nanocrystals were tested in comparison with CdSe/ZnS nanocrystals.

Then, using the indigenously developed anhydrous synthesis procedure in methanol, core/shell nanocrystals of cerium-doped lanthanum bromide/undoped lanthanum fluoride were successfully synthesized. All samples were subject to basic structural and optical characterization that included imaging using transmission electron microscope, energy dispersive spectroscopy, absorption measurements, excitation and emission photoluminescence spectroscopy, and photoluminescence lifetime measurements.

Table of contents

Pages

List of figures

List of tables

LIST OF PUBLICATIONS

1. M. Osiński, K. Sankar, B. A. Akins, T. A. Memon, N. J. Withers, and G. A. Smolyakov, "*Synthesis and characterization of ZnO/ZnS core/shell nanocrystals*", Invited Paper, Proceedings of the 2007 US-Korea Conference on Science, Technology, and Entrepreneurship (UKC2007), Global Challenges in Science and Technology, Symposium NST: Nano Science and Technology, Reston, Virginia, 9-12 August 2007, Paper NST-7.2.

2. K. Sankar, B. A. Akins, T. A. Memon, N. J. Withers, S. T. Bowers, T.-Y. Gu, J.-J. Gu, M. R. Greenberg, G. A. Smolyakov, and M. Osiński, "*Colloidal synthesis and characterization of optically active ZnO/ZnS core/shell nanocrystals*", Symposium L: Zinc Oxide and Related Materials, 2007 MRS Fall Meeting, Boston, Massachusetts, 26-30 November 2007, MRS Symposium Proceedings, Vol. 1035E, Paper L11.12 (available online).

3. N. J. Withers, K. Sankar, B. A. Akins, T. A. Memon, J.-J. Gu, T.-Y. Gu, S. T. Bowers, M. R. Greenberg, G. A. Smolyakov, R. D. Busch, and M. Osiński, "*Effects of gamma irradiation on optical properties of colloidal nanocrystals*", Symposium O: Nuclear Radiation Detection Materials (D. L. Perry, A. Burger, L. Franks, and M. Schieber, Eds.), 2007 MRS Fall Meeting, Boston, Massachusetts, 26-30 November 2007, MRS Symposium Proceedings, Vol. 1038, Paper O9.5 (in print).

4. K. Sankar, B. A. Akins, T. A. Memon, N. J. Withers, G. A. Smolyakov, and M. Osiński, "*Synthesis and characterization of scintillating lead-iodide-based nanocrystals*", Colloidal Quantum Dots for Biomedical Applications III (M. Osiński, T. M. Jovin, and K. Yamamoto, Eds.), SPIE International Symposium on Biomedical Optics BiOS 2008, San Jose, California, 19-21 January 2008, Proceedings of SPIE, Vol. 6866, pp. 686604-1 – 686604-12.

5. N. J. Withers, K. Sankar, T. A. Memon, B. A. Akins, J.-J. Gu, T.-Y. Gu, G. A. Smolyakov, and M. Osiński, "*Fast-decay-time scintillation of LaF_3:Ce colloidal nanocrystals*", Technical Digest CD-ROM, Twenty Eighth Annual Conference on Lasers and Electro-Optics CLEO 2008, San Jose, California, 5-9 May 2008, Paper CWM6.

6. N. J. Withers, K. Sankar, B. A. Akins, T. A. Memon, T.-Y. Gu, J.-J. Gu, G. A. Smolyakov, and M. Osiński, "*Effects of gamma irradiation on optical properties of CdSe/ZnS colloidal quantum dots*", Technical Digest CD-ROM, Twenty Eighth Annual Conference on Lasers and Electro-Optics CLEO 2008, San Jose, California, 5-9 May 2008, Paper JThA66.

7. N. J. Withers, K. Sankar, B. A. Akins, T. A. Memon, T.-Y. Gu, J.- J. Gu, G. A. Smolyakov, M. R. Greenberg, T. J. Boyle, and M. Osiński, "*Rapid degradation of CdSe/ZnS colloidal quantum dots exposed to gamma irradiation*", Applied Physics Letters 93 (2008): 173101.

8. N. J. Withers, K. Sankar, B. A. Akins, T. A. Memon, J.-J. Gu, T.-Y. Gu, G. A. Smolyakov, R. D. Busch, and M, Osiński, "*Synthesis and characterization of* LaF_3*:5%*Ce^{3+} *scintillating nanocrystals*", submitted to IEEE Transactions on Nuclear Science.

9. K. Sankar, B. A. Akins, T. A. Memon, N. J. Withers, G. A. Smolyakov, and M. Osiński, "*Synthesis and characterization of scintillating cerium-doped lanthanum fluoride nanocrystals*", accepted for Colloidal Quantum Dots for Biomedical Applications IV (M. Osiński, T. M. Jovin, and K. Yamamoto, Eds.), SPIE International Symposium on Biomedical Optics BiOS 2009, San Jose, California, 24-26 January 2009.

10. N. J. Withers, N. D. Triño, K. Sankar, B. A. Akins, A. C. Rivera, G. A. Smolyakov, G. S. Timmins, M. Osiński, "*Scintillating-nanoparticle-induced enhancement of radiation damage in living cells*", accepted for Colloidal Quantum Dots for Biomedical Applications IV (M. Osiński, T. M. Jovin, and K. Yamamoto, Eds.), SPIE International Symposium on Biomedical Optics BiOS 2009, San Jose, California, 24-26 January 2009.

11. S. McGill, C. Cuylear, T. Memon, A. Jakus, B. A. Akins, K. Sankar, M. Osiński, H. D. Smyth, "*Enhanced drug transport through alginate biofilms using magnetic nanoparticles*", accepted for Colloidal Quantum Dots for Biomedical Applications IV (M. Osiński, T. M. Jovin, and K. Yamamoto, Eds.), SPIE International Symposium on Biomedical Optics BiOS 2009, San Jose, California, 24-26 January 2009.

12. N. J. Withers, K. Sankar, J. B. Plumley, A. C. Rivera, B. A. Akins, G. A. Smolyakov, and M. Osiński, "Lanthanide-halide-based nanoscintillators for portable radiological detectors", submitted to Optics and Photonics in Global Homeland Security V (C. S. Halvorson and Š. O. Southern, Eds.), SPIE Defense, Security, and Sensing Symposium, Orlando, Florida, 13-17 April 2009.

13. N. J. Withers, K. Sankar, J. B. Plumley, B. A. Akins, T. A. Memon, A. C. Rivera, G. A. Smolyakov, and M. Osiński, "Optimization of Ce content in $Ce_xLa_{1-x}F_3$ colloidal nanocrystals for gamma radiation detection", submitted to Symposium L: Nuclear Radiation Detection Materials, 2009 MRS Spring Meeting, San Francisco, California, 13-17 April 2009.

14. K. Sankar, J. B. Plumley, A. C. Rivera, B. A. Akins, T. A. Memon, N. J. Withers, G. A. Smolyakov, and M. Osiński, "Optical properties of hygroscopic core/stable shell $LaBr_3$:Ce/LaF_3 colloidal nanocrystals for detection of ionizing radiation", submitted to Twenty Ninth Annual Conference on Lasers and Electro-Optics CLEO 2009, Baltimore, Maryland, 31 May – 5 June 2009.

LIST OF PROVISIONAL PATENT APPLICATIONS

1. M. Osiński, N. J. Withers, B. A. Akins, G. A. Smolyakov, and K. Sankar, "*Lead-halide-based scintillator materials*", United States Provisional Patent Application 61/072,636 filed on 31 March 2008.

2. M. Osiński, K. Sankar, B. A. Akins, G. A. Smolyakov, and N. J. Withers, "*Lanthanide-halide core/shell scintillator materials*", United States Provisional Patent Application 61/046,035 filed on 18 April 2008.

Chapter 1

Introduction

1.1. Nanocrystals: Properties and advantages

A nanocrystal is a material whose size is on the order of nanometers. The idea behind realizing particles of nanometer size is to achieve quantum confinement. Quantum confinement occurs when electron and hole wavefunctions in a material are restricted in one or more dimensions. That is, quantum confinement occurs when one or more of the dimensions of nanocrystals are made very small so that they approach the size of an exciton in a bulk semiconductor crystal, called the Bohr exciton radius.

A quantum well is a structure whose height is approximately the Bohr exciton radius while the length and width can be large. A quantum wire is a structure where the height and width are made small while the length can be long. A quantum dot is a structure where all dimensions are near the Bohr exciton radius, typically a small sphere. Specifically, as the size of the crystal reaches quantum confinement levels, the energy levels in the valence and conduction bands of the material become discrete, as opposed to being continuous in the bulk material. This means that the energy levels are separated by enough energy that the addition or subtraction of few atoms or electrons to the crystal will measurably change the energy of the bandgap. It is when a crystal has discrete energy states that it can be defined as a nanocrystal, and this is when it takes on useful and interesting properties (Blasse and Grabmaier 1994). This means that nanocrystals can emit at different (and specifiable, to within limits) wavelengths. This predictability of

emission and tunability would be impossible with a traditional semiconductor with continuous energy levels.

Due to the similarity between the discrete energy levels of quantum dots and the discrete energy levels of atoms, nanocrystals are often thought of as artificial atoms. Since the energy levels are determined by the size of the nanocrystal, they can be tuned in a controlled way by synthesizing nanocrystals of different diameters. For semiconductor nanocrystals, this involves a size-dependent bandgap. Analogous to atoms, charge carriers are excited to upper energy levels if nanocrystals are excited optically. If, as is the case for many semiconductors, the bandgap of the bulk semiconductor is in the near infrared, the wavelength of the fluorescence light emitted when excited charge carriers fall back to the ground state will be in the visible spectral range. The smaller the nanocrystal is, the larger the spacing between the energy levels and therefore the larger the energy gap and, thus, the shorter the wavelength of the fluorescence. One other major advantage of producing nano-scaled crystals is the significant reduction in crystal defects. Since the probability of crystal/lattice defects is proportional to the size of the crystal, nanocrystals are by far less susceptible to defects in comparison with bulk crystals. This enables facile production of high-quality luminescent nanosized crystals.

1.2. Inorganic luminescent nanocrystals and their applications

Inorganic nanocrystals exhibit many interesting size and shape dependent properties based on which many new potential applications can be explored (Parak *et al.* 2003). One of the most important properties of semiconductor nanocrystals is the variation of bandgap as a function of size. As explained above, according to quantum confinement theory, higher energy photons are required to excite electrons from the

valence band to the conduction band at smaller volumes of the crystal. Therefore, by varying size and composition of nanocrystals, the luminescent emission can be tuned from red at 6 nm to blue at 5 nm size of the same semiconductor nanocrystal (Figure 1.1). The unique photophysical properties of fluorescent nanocrystals make them very attractive as biological probes for molecular recognition, fluorescent labeling of biological cells, DNA sorting, *etc.* (Parak *et al.* 2003). Other potential applications include nanophosphors for solid-state lighting and display, and ionizing radiation detection.

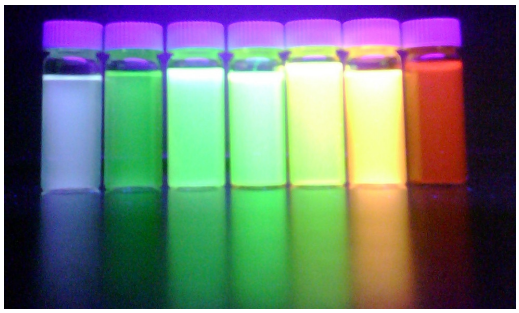

Figure 1.1: CdSe NCs of different sizes, synthesized at CHTM, fluorescing with different colors under UV excitation

1.2.1. Current application: Biological fluorescent labeling

One of the most powerful tools available to the biologist is fluorescent labeling. A molecule that emits light can be attached to a specific bio-molecule, and then the fluorescence can be used to image the location of the molecule or to probe its environment. Quantum dots potentially offer significant advantages over conventional light-emitting biological probes (Han *et al.* 2001), (Rosenthal 2001). Unlike molecular bio-labels, the colloidal quantum dots can all be excited with a single excitation source. For example, the "actin" protein fibers of a mouse fibroblast cell can be labeled with

larger size, red emitting dots, while the cell nuclei can be labeled with smaller, green emitting dots so that the cell structure can be observed with clear distinction using the same fluorescent labeling material (Parak *et al.* 2003). Furthermore, a major need in biological analysis is the ability to detect multiple optical signals simultaneously. For instance, cell biologists sort populations of cells according to which combination of several antibodies will bind to them.

Molecular biologists would like to screen for the presence of numerous DNA sequences simultaneously. Combinations of conventional fluorescent tags are not well suited to these tasks, since they are molecules with discrete energy levels, and each one must be excited at resonance. Semiconductor quantum dots emit light at a specific energy determined by size and composition; however, like in a bulk semiconductor, when tuned above the threshold for absorption, more and more channels for absorption of photons open up, so that the excitation spectrum is essentially continuous. Thus, combinations of emitting colors can readily be excited with a single excitation source. The colloidal nanocrystal emission is narrower and more symmetric than that of the organic dyes, potentially allowing a larger number of probes within a detectable spectral region. The efficacy of using water-soluble core/shell colloidal nanocrystals for two-color fluorescent biological labeling has been demonstrated, and many related applications are now actively under investigation (Parak *et al.* 2003).

An interesting biotechnology application of nanophosphors is molecular bio-imaging through up-conversion. In general terms, up-conversion refers to the conversion of longer wavelength light to shorter wavelength light (Rosenthal 2001). Bio-molecules and cells are tagged to compounds that luminesce when exposed to either visible or

ultraviolet light. Such shorter wavelengths can potentially destroy the sample material quickly. Using the up-converting nanophosphors to tag and visualize the DNA, for example, may provide an advantage because the nanophosphors can be activated by infrared light, which is less harmful than ultraviolet or visible light.

1.2.2. Potential application: Nanophosphors for solid-state lighting

It is established that, for nanocrystals confined in three dimensions, absorbance and emission spectra are defined by the size and surface chemistry of the crystal. For sufficiently small crystals, the effect of size-dependent quantum confinement on absorption and the large role that the surface molecules play in the emission allows the decoupling of the two optical properties. Due to this property of tunability, quantum dots have almost negligible self-absorbance of their emitted light (Chander 2005). Since for small nanocrystals, almost 70 percent of the atoms are at the surface, specific emission can be obtained by making simple changes in the interface passivation of the crystals. Furthermore, by growing the crystals to a specific size, the absorbance edge can be adjusted to match with the wavelength of the UV or blue LED used in solid-state lighting. Therefore, it is possible to synthesize quantum dots of very high quantum efficiency suitable for use as nanophosphors for solid-state lighting.

The main requirements for a material to be good for solid-state lighting are emission efficiency, negligible emission quenching, and absence of defects and surface trap sites. For this reason, a new class of nanocrystals where luminescent ions are doped in a wide-bandgap host material proves to be attractive for solid-state lighting. Ideally, when high-efficiency photoluminescent ions are doped in low vibrational energy lattice

host material and coated with an undoped wide-bandgap material, the luminescence efficiency is at its best. Yet another major advantage of nanophosphors is their small particle size, which significantly reduces internal scattering effects in comparison to bulk phosphors, and improves the performance when nanophosphors are coated on LEDs used for solid-state lighting (Chander 2005).

1.2.3. Potential application: High-energy ionizing radiation detection

One of the emerging and high-potential applications of nanocrystals is in the field of high-energy-ionizing radiation detection. Substances that absorb high-energy ionizing electromagnetic or charged-particle radiation and in response release the absorbed energy by fluorescing at a characteristic emission wavelength, known as scintillators, are important materials for radiation detection applications. Chief characteristic requirements of scintillators are high conversion efficiency, meaning number of photons emitted per electronvolt of energy absorbed, short luminescence decay time, good energy resolution, and transparency at the wavelength of emission. Among many varieties such as organic, plastic, and inorganic scintillators, the latter are usually known for their high stopping power, since high atomic weight inorganic compounds are available that also have high light yield. A new species of nanocrystals, where a highly luminescent ion is doped into a wide-bandgap host matrix is attractive for high-energy ionizing radiation detection. Since lanthanides are excellent luminescent ions, and lanthanide halides are good wide-bandgap host materials, they are popular known as lanthanide-doped lanthanum halide nanocrystals, which are very good candidates for radiation detection applications. For detection of high-energy particles such as alpha and beta particles, the radiation must be

sufficiently slowed down so as to facilitate its interaction with the scintillator atoms and eventually resulting in absorption of the energy. Therefore, high density is a key characteristic of high-energy radiation scintillators. Over the years, one of the key inadequacies of inorganic scintillators is their relatively poor energy resolution.

1.2.3.1. Process of gamma-ray scintillation detection

As described by Chen and Belbot, the process of detecting a gamma ray photon can be elaborated in the following steps (Chen and Belbot 2005). A gamma-ray photon interacts with the scintillator and transfers part or all of its energy to one or more atomic electrons. The fast electron travels on, ionizing and exciting the scintillation material. Some molecules or crystal lattices go to excited states and when returning to lower-energy states (such as ground state) they may emit a light photon. Positrons may also be involved, with similar final effect. Depending on whether the crystal is pure or doped, the light yield may vary. Most of the ionization/ excitation results in no light being produced. Usually only one surface of the scintillator is designed to allow light out, while others are coated with diffusive reflector material, as shown in Figure 1.2. Scintillation light is isotropic. The diffusive reflector increases a chance that the photons will be redirected towards the photoelectric detector, usually a vacuum tube with multiple cathodes and an anode called the photomultiplier tube (PMT). At the exit surface of the scintillator, light has only a partial chance to come out, because the refractive indices do not match. A fraction of the photons will eventually travel into the PMT glass window. The emerged light photons hit the PMT cathode and some will generate photoelectrons. Cathode is

usually a thin layer of bi-alkali material coated on the vacuum-side surface of the entrance window. The quantum efficiency is generally 20%-30%.

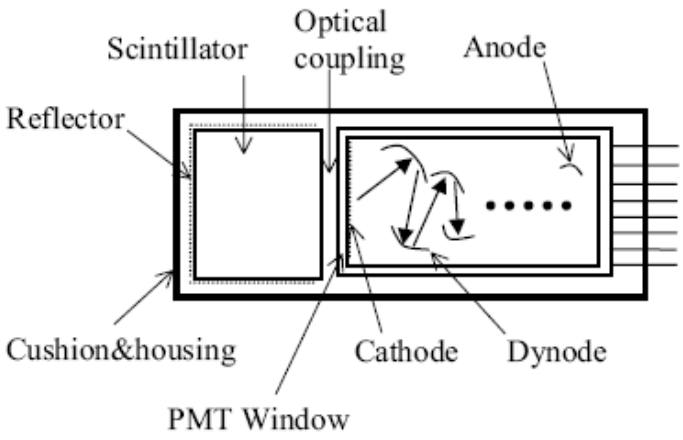

Figure 1.2: Structure of a typical spectroscopic scintillation detector (Chen and Belbot 2005)

Subsequently, the photoelectrons are amplified by the PMT, which usually has 8 or 10 stages, with each stage operating at 3-4 times amplification. In PMTs with focusing, the first dynode catches most of the cathode electrons. The anode (last stage) electrons are collected, forming an electronic pulse. The signal amplitude (total area) is proportional to the energy deposited into the scintillator. From ionization to excitation, to light emission, to light collection, and to cathode electron, it is a cascade of binomial processes. Since the probability that ionization leads to a light photon and eventually leads to a cathode electron is small, the cathode electron number has a Poisson distribution. Further, the average cathode electron number is statistically large enough to be considered a Gaussian distribution, whose variance equals its mean value and its standard deviation equals the square root of its mean (Chen and Belbot 2005).

1.2.3.2. Requirements of a good scintillator material

Optimal requirements of a good scintillator material are: (i) fast response time (10-100 ns or faster) and fast signal rise time for good time resolution and handling of high counting rates, (ii) high light yield (>50,000 photons per MeV of absorbed gamma ray energy) for good energy, time, and position resolution, (iii) proportional response for good energy resolution, (iv) high density, ρ, high atomic number, *Z*, for high gamma ray detection efficiency, (v) emission wavelength matching the detector response, and (vi) last but not least, low cost and ease of large-scale manufacturability. This work will be discussing the synthesis and characterization of nanomaterials that have primary potential as high-energy scintillation detectors, focusing on characteristics such as high stopping power, high-energy resolution, and fast decay times.

1.3. Background and motivation

The recent interest and motivation to study lanthanide or rare-earth-doped heavy-metal halide compounds has been primarily due to the new material requirements of applications such as improved LEDs, biological markers, nuclear medical imaging such as positron emission tomography (PET), and ionizing radiation detectors or scintillators. These applications require materials that have significantly higher light yield and fewer material defects to yield high-performance. The high-energy ionizing radiation detection is of particular interest and relevance to this work. Scintillation is the process of absorption of ionizing radiation by the material and subsequent emission of photons in a pulse whose total energy is directly related to the energy of the absorbed photon. Since, the emission and absorption processes are temporally separated at the order of

nanoseconds, the light emission occurs in burst-like events that appear as light pulses, and hence the name scintillation.

In an effort to design a material suitable for detection of ionizing radiation, certain conditions have to be satisfied. Since ionizing radiation is usually of the order of high-energy, firstly, the material must be capable of absorbing high-energy radiation. Photoelectrons or secondary electrons created in the process travel at high velocities. And, for energy transfer to take place between these particles and the atoms of the scintillating material, they must be slowed down sufficiently to allow the interaction to occur. Therefore, high atomic weight and high density material capable of attenuating the radiation is required. Most importantly, a material that characteristically emits in the near UV or visible wavelength with high efficiency is required to be intrinsically situated or doped within a wider bandgap material/host. Ideally, this material, known as activator, traps the excited carriers from the host and emits light after carrier relaxation in its internal energy levels. Furthermore, the time to emission or the carrier relaxation time is important since materials that emit faster after absorption can provide higher rates of detection and therefore better accuracy. For this specific purpose, mainly of interest in PET scanning application, a material that has a fast decay time will be useful. Essentially, a fast, single emission line, high light output activator species embedded in a high density, high molecular weight, and wide bandgap host should prove to be an ideal scintillator material for ionizing radiation detection applications.

The requirements of other applications such as phosphors in light emitting devices and markers in biological imaging also overlap with such properties. As already mentioned, for a material to be a good phosphor would require it to be a highly efficient

light emitter mostly free from crystal defects. Therefore, it will be useful to have the luminescent center in a wide bandgap material that will significantly improve the quantum yield by providing a rigid crystal host environment (Kompe *et al.* 2003).

In summary, the optimal requirements for a good scintillator material are: (i) fast response time (10-100 ns) and fast signal rise time for good time resolution and handling of high counting rates, (ii) high light yield (>50,000 photons per MeV of absorbed gamma ray energy) for good energy, time, and position resolution, (iii) proportional response for good energy resolution, (iv) high density, ρ, atomic weight, *Z*, for high gamma ray absorption efficiency, (v) emission wavelength matching the detector response, and (vi) last but not least, low cost and ease of large-scale manufacturability (Krämer *et al.* 2006).

1.3.1. Limitations of early radiation detectors

Radiation detectors developed initially suffered from marked limitations as illustrated in the table below:

Table 1.1: Properties of common radiation detector materials (Derenzo 2005)

Semiconductor material	**Density**	**Att. length (for 511 keV) (mm)**	**Light yield (for 511 keV)**	**Bandgap (eV)**
Silicon	2.33	44.6	0.0016	1.12 (I)
LN-cooled germanium	5.35	23.7	0.043	0.67 (I)
Cadmium zinc telluride	5.76	20.1	0.18	1.7 (I)
LN-cooled lead iodide	6.16	14.1	0.4	2.4 (D)
Aluminum antimonide	4.22	27.2	0.16	1.6 (I)

Although liquid-nitrogen (LN)-cooled germanium, cadmium zinc telluride, and LN-cooled lead iodide have good density and reasonable attenuation length, the light yield is

considerably low and they also have a narrow bandgap. Inorganic scintillating materials were developed subsequently.

1.3.2. Inorganic scintillator materials

Since 1990, many new bulk crystals of various inorganic scintillator materials have been discovered, manufactured, and studied, as shown in Figure 1.3, courtesy of Marv Weber (Derenzo 2005):

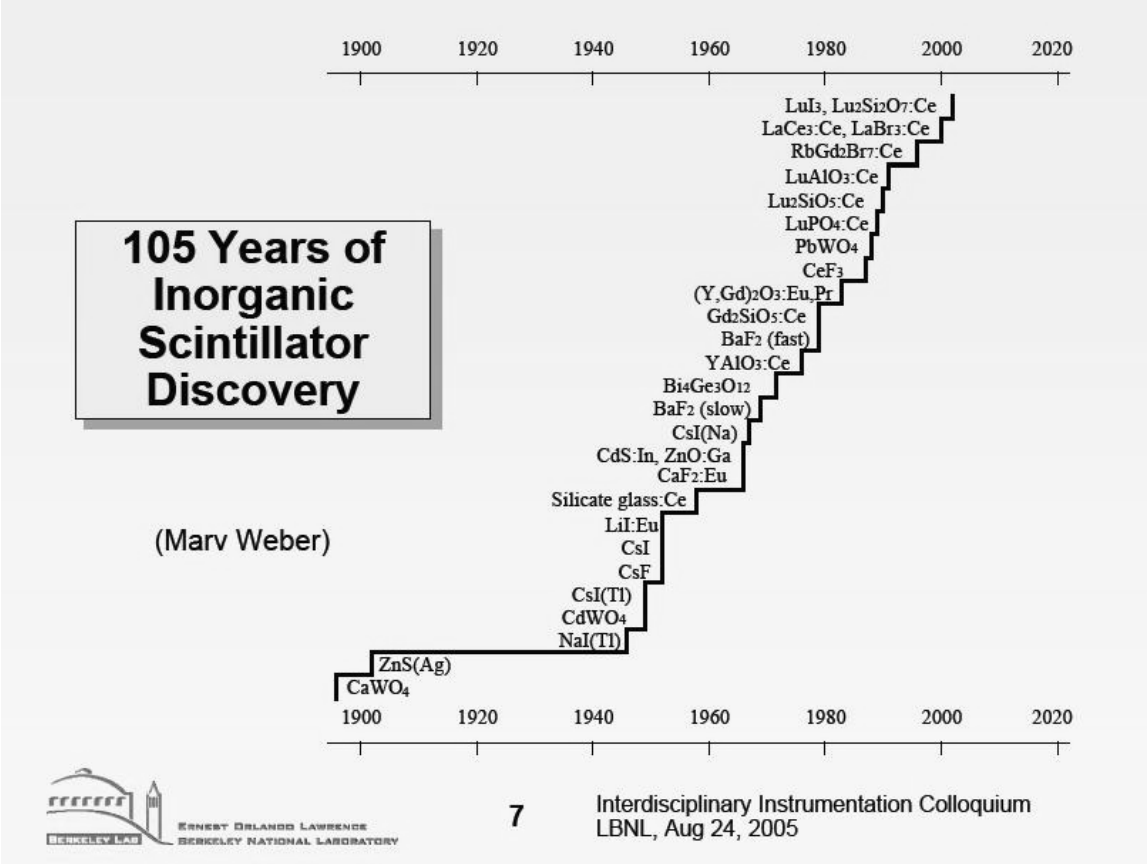

Figure 1.3: History of scintillator material discovery (Derenzo 2005)

Scintillating crystals developed between 1940-1990, such as $Bi_4Ge_3O_{12}$(BGO), NaI(Tl), BaF_2, Lu_2SiO_5:Ce (LSO) were better than semiconductor materials, but suffered from

various limitations like poor light yield, long decay lifetime, low energy resolution, and/or high cost.

1.3.3. Cerium-doped scintillator materials

Cerium-doped bulk lanthanum halide compounds are attractive due to their interesting properties that include efficient radiation absorption, highly luminescent activator (cerium), emission through molecular transitions, host to protect activators from luminescence quenching, and fast decay time of radiative transitions between cerium levels (20-40 ns). A notable fact is that the cerium ion (among few lanthanide ions), has the wavelength of its first excited state higher than the 180 nm (55000 cm^{-1}) transmission cut off of air (Heaps *et al.* 1976). Among a variety of cerium-doped bulk crystals that possessed good scintillation detection properties. Cerium doping of bulk lanthanum bromide was reported to have a light yield of 60,000 photons/MeV, 2.5% full-width-to-half-maximum energy resolution (variation in emission light yield to absorbed gamma energy) for 662 keV gamma rays, 25 ns short decay time, and a density of 5.3 g/cm^3 with 22 mm attenuation length for 511 keV gamma rays (Derenzo *et al.*). However, the crystals are hygroscopic and very fragile, and hence have to be protected from external environment both during growth and use.

In spite of being the ideal material for ionizing radiation detection, cerium-doped lanthanum bromide bulk crystals are expensive and difficult to manufacture and use. Therefore, the underlying motivation of this work is to develop cerium-doped lanthanum bromide colloidal nanocrystals coated with a stable lanthanum fluoride shell. Lanthanum fluoride, a stable material, having a higher bandgap (10.2 eV) compared to lanthanum bromide (5.15 eV), and also being very similar to lanthanum bromide from a

crystallographic point of view, is the most logical choice for the shell material to coat the highly hygroscopic lanthanum bromide nanocrystals.

1.4. Objective and scope of thesis

As the first step, cerium-doped lanthanum fluoride core-only colloidal NCs were synthesized using two different synthesis routes, in water and in anhydrous methanol (water-free), respectively. The optimum cerium concentration and radiation hardness of these NCs were determined. Then, using the water-free route, cerium-doped lanthanum fluoride/undoped lanthanum fluoride core/shell NCs were synthesized. Using a similar water-free procedure cerium-doped lanthanum bromide core-only NCs were synthesized in argon environment. Finally, core/shell colloidal NCs of cerium-doped lanthanum bromide/undoped lanthanum fluoride NCs were synthesized.

The first chapter of this thesis provides introduction on colloidal nanocrystals, the background, and motivation to pursue cerium-doped lanthanum halide nanocrystals. The second chapter deals with the description of the approach to wet chemical synthesis routes and to the structural and optical characterization methods used in this work. The third chapter details the aqueous synthesis and characterization of cerium-doped lanthanum fluoride core colloidal nanocrystals in water, while the fourth chapter details the indigenously developed anhydrous synthesis and characterization of cerium-doped lanthanum fluoride/undoped lanthanum fluoride core/shell colloidal NCs. The fifth and sixth subsequent chapters describe the optimization of cerium concentration in cerium-doped lanthanum fluoride NCs, and radiation hardness testing experiments, respectively. The seventh chapter deals with the synthesis and characterization of cerium-doped

lanthanum bromide core and cerium-doped lanthanum bromide/undoped lanthanum fluoride core/shell colloidal NCs. The last chapter concludes this work and also provides some insights on potential future work.

References

1. Blasse, G., and B. C. Grabmaier. *Luminescent Materials,* Berlin: Springer, 1994.
2. Chen, G. Y., and M. Belbot. "Improving energy resolution of scintillation detectors" *Nuclear Science Symposium.* IEEE, (2005) 235-238.
3. Chander, H. "Development of nanophosphors-A review." *Materials Science and Engineering: Report* 16, no. 5 (2005): 113-155.
4. Derenzo, S. E. "Who needs better nuclear detector materials and how do we find them?" *Interdisciplinary Instrumentation Colloquium.* Berkeley: Ernest Orlando Lawrence Berkeley National Laboratory, (2005).
5. Han, M. Y., X. H. Gao, X. H. Su, and S. Nie. "Quantum-dot-tagged microbeads for multiplexed optical coding of biomolecules" *Nature Biotechnology,* 19 (2001): 631-635.
6. Heaps, Wm. S., L. R. Elias, and L. M. Yen "Vacuum-ultraviolet absorption bands of trivalent lanthanides in LaF_3" *Phys. Rev. B.,* 13, no. 1 (1976): 94-99.
7. Jia, D. D. "Nanophosphors for white LEDs" Chemical Engineering Communications, 194, no. 13 (2003): 5513-5516.
8. Kompe, K., H. Borchert, J. Storz, S. Adam, T. Moller, and M. Haase. "Green-emitting $CePO_4$:Tb/$LaPO_4$ core–shell nanoparticles with 70% photoluminescence quantum yield" *Angew. Chem.* 42, no. 5 (2003): 5513-5516.
9. Kramer, K. W., P. Dorenbos, H. U. Gudela, and C. W. E. van Eijk. "Development and characterization of highly efficient new cerium-doped rare earth halide scintillator materials" *Journal of Materials Chemistry 18, no. 12*, (2006): 2773-2780.
10. Parak, W. J., D. Gerion, T. Pellegrino. "Biological applications of colloidal nanocrystals" *Nanotechnology,* 14 (2003): 123-129.
11. Rosenthal, S. J. "Bar-coding biomolecules with fluorescent nanocrystals" *Nature Biotechnology* 19, no. 3 (2001): 621-622.

Chapter 2

Approach to synthesis, structural, and optical characterization of colloidal nanocrystals

2.1. Introduction to colloidal nanoscale synthesis

Some of the major techniques to manufacture quantum-confined nanosized crystals are molecular beam epitaxy and metal organic chemical vapor deposition, combustion synthesis, sol-gel approach, high-temperature solvent-based wet chemical approach, and low-temperature aqueous precipitation method. The latter three techniques can be classified under bottom-up colloidal synthesis routes. High-temperature solution-grown approach has been used extensively for synthesizing highly crystalline and monodisperse II-VI nanocrystals, such as CdSe and CdS over a wide size range. This has been quite successfully extended to III-V materials to produce high quality ZnO, InP, InN, and InAs nanocrystals. Generally, coordinating or non-coordinating solvents that have high boiling point are used to carry out the reaction at elevated temperatures. The precursors are injected rapidly at the reaction temperature, and the nanoparticles are formed, allowed to grow, collected, and dispersed in appropriate media. In cases where high temperature is not required for the reaction, direct aqueous synthesis can be carried out at low temperatures using precipitation technique. Wang *et al.* have reported a successful low-temperature aqueous synthesis of europium-doped lanthanum fluoride nanocrystals (Wang *et al.* 2006).

2.1.1. Colloidal synthesis setup and general procedures

For synthesis of colloidal nanocrystals using wet chemical bottom-up approach, the entire reaction needs to be conducted in an inert atmosphere, which will enable handling of air-sensitive precursors, remove any possibility of contamination and/or oxidation of the produced nanocrystals, and also provide for the removal of any gas byproducts from the reaction. For this purpose, a specialized laboratory glassware system known as Schlenk line is used, which provides a controlled pressure, and pure argon (inert) atmosphere for the reaction. The Schlenk line contains two independent lines for vacuum and inert gas as shown in Figure 2.1.

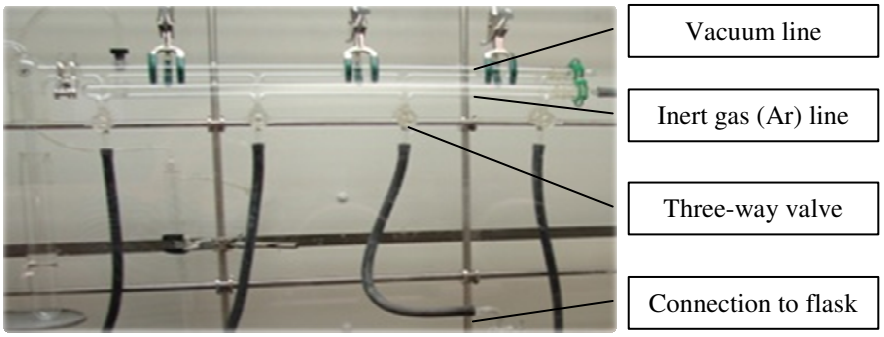

Figure 2.1: Photograph of the Schlenk line apparatus

Three-way valves facilitate online switching between the lines during the reaction, if needed. The reaction flask is a three-neck round-bottom flask with the center neck usually connected to one of the lines on the Schlenk line. The other two necks are sealed using rubber septa, with one septum used for inserting a thermocouple. The thermocouple is in turn connected to a closed-loop p-i-d ramping temperature controller. For continuous stirring of the solution in the flask, the flask contains a small cylindrical teflon-coated stir

bar, which is spun using a rotating magnetic field generated by a stirring controller placed beneath the heating mantle. The round-bottom flask is placed firmly on top of the heating mantle, ensuring a good thermal contact. A schematic of the above mentioned setup is shown in Figure 2.2.

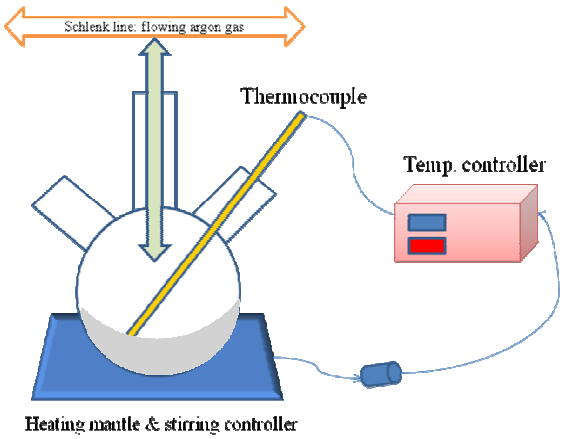

Figure 2.2: Schematic representation of colloidal synthesis setup

To enable handling of air-sensitive chemicals and processes, the MBraun UNILab^{TM} glovebox pressurized with ultra-pure argon at 4-8 bar was used. Gloves are provided for handling chemicals and equipment, while antechamber ports are used to transfer chemicals and equipment from/into the box.

All glassware was cleaned using a typical laboratory glassware cleaning procedure, according to which it was first treated with dilute base, rinsed with water, placed in an acid bath, and then rinsed with water again. Typical chemical laboratory safety standards, such as wearing safety goggles or face shield, lab coats, appropriate gloves, full pants, and toe-covered shoes were adhered to while carrying out synthesis procedures. The colloidal synthesis lab was fully equipped with air-quality sensor, gas alarm, eyewash, and chemical spill-kits readily available in case of accidents or emergencies.

2.1.2. Introduction to colloids and advantages of colloidal approach

Colloid or colloidal dispersion is a heterogeneous mixture that visually appears to be a homogeneous solution. A heterogeneous mixture is a mixture of two phases, such as a solid and a liquid phase. In a colloid, the dispersed phase is made of tiny particles that are distributed evenly throughout the continuous liquid phase. In nature, colloids are present in various forms around us but are rarely recognized. Some examples of popular colloids are milk, dust particles in air, smoke, paint, cheese, jelly, whipped cream, styrofoam, fog, clouds, *etc*. Among many types of colloids such as aerosols, gels, foams, emulsions, and sols or colloidal dispersions, there are several facile methods to synthesize and characterize colloidal nanocrystal dispersions. Colloidal nanocrystals are nanometer-sized, solution-grown inorganic particles stabilized by a layer of surfactants attached to their surface. Basically, there are two methods to produce nanosized crystals. First is to manufacture a large crystal and break it up into pieces as small as few nanometers. The major disadvantage of this approach is the inability to produce a good size distribution, which in turn produces a broad emission line due to size dependent emission that defeats the purpose of nanocrystals, which are expected to have a narrow emission line at a characteristic wavelength. The second method is to produce the crystals chemically, using the bottom-up approach. This involves precisely controlling a chemical reaction that will enable to control and stop a reaction at the time of the product formation, so that crystal growth can be interrupted at the very initial phases and nano-sized crystals can be thus produced.

Compared to other techniques, the chemically grown colloidal nanocrystals present several advantages. Just the simplicity of performing chemical reactions at

controlled conditions makes the entire process easy, cheap and repeatable, which is a major advantage in light of large-scale manufacturing potential of the nanoparticles. Furthermore, the preparation of nanocrystalline samples that are uniform in size, composition, shape, internal structure, and surface chemistry enables mapping of their size-dependent material properties. The high-temperature solution phase synthesis of colloidal nanocrystal dispersions provides a method to prepare such uniform nanocrystalline samples for a variety of metals and semiconductors (Murray *et al.* 2001).

2.1.3. Mechanism of chemical reaction and size control

Chemical reactions convert reactants possessing well defined properties into materials with different properties that are known as products. The change in concentration of reactants or products per unit time is called reaction rate. In general, the factors affecting reaction rate are physical state of the reactants, concentration of reactants, temperature, and catalysts (Brown *et al.* 2006). At the molecular level, the rate of reaction depends on the frequency of collisions between molecules with sufficient energy, which is the case in the synthesis of nanocrystals.

Nanocrystals consist of an inorganic core (<100 atoms) and may contain organic surfactants that stabilize the core, passivate against oxidation, and prevent agglomeration. The syntheses of colloidal nanocrystals occur in three stages; nucleation, growth, and Ostwald ripening. The factors controlling these stages are concentration and chemistry of reagents and surfactants, temperature, growth time, and surfactant to reagent ratio. Monodisperse nanocrystals can be obtained by rapid injections of reagents into a reaction vessel containing a hot, coordinating solvent (Murray *et al.* 1993). This high-temperature

solvent decomposes the reagents, forming a supersaturation of these molecules in solution. After subsequent nucleation of products, the concentration of the reactant species drops below the critical concentration for nucleation. Therefore, further addition of material will only add to the existing nuclei, resulting in the growth of the nanocrystals, as shown by the flowchart in Figure 2.3.

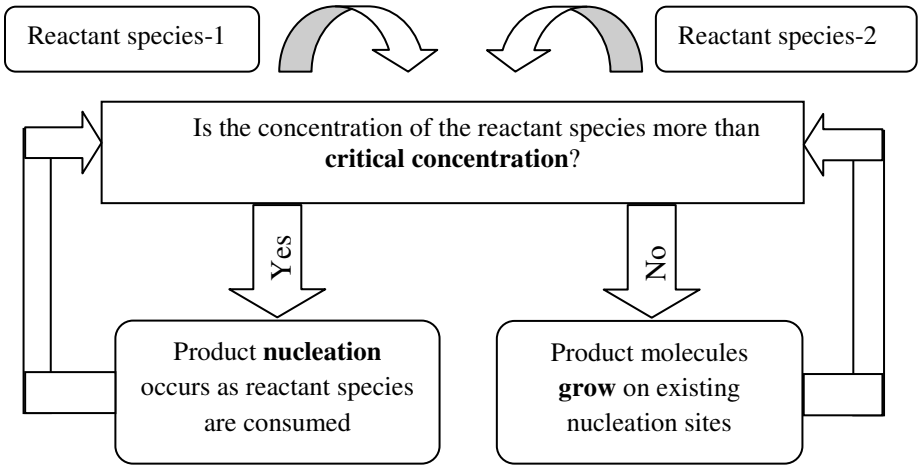

Figure 2.3: Flowchart describing the nucleation and growth steps in a chemical reaction

An alternative synthetic approach involves mixing the reagents in the vessel at a temperature low enough to prevent any possible reaction from occurring. A controlled ramp of solution temperature accelerates the chemical reaction and produces the requisite supersaturation, which is then relieved by a burst of nucleation (Murray *et al.* 2001). Later on, a uniform surface regularity in core structure can be achieved through slow growth and annealing of these nanoparticles in the coordinating solvent. Many systems also exhibit a second, distinct, growth stage known as Ostwald ripening, in which the high surface energy of the smaller nanocrystals promotes their dissolution and the materials redeposit on the larger nanocrystals. Ostwald ripening is an observed phenomenon in solid (or liquid) solutions, which describes the evolution of an

inhomogeneous structure over time. This thermodynamically driven spontaneous process occurs because larger particles are more energetically favored than smaller particles (Vengrenovich *et al.* 2001). This stems from the fact that molecules on the surface of a particle are energetically less stable than the ones already well ordered and packed in the interior. Larger particles, with their lower surface to volume ratio, are in a lower energy state (and have a lower surface energy). As the system tries to lower its overall energy, molecules on the surface of a small (energetically unfavorable) particle will tend to diffuse through solution and add to the surface of larger particles (Ratke and Voorhees 2002). A critical size exists for a given initial concentration of the reactant species. Nanocrystals, that are smaller than the critical size start dissolving, while the larger ones keep growing. In the process, many smaller crystals formed initially slowly disappear, except for a few that grow larger, at the expense of the smaller crystals. The smaller crystals act as fuel for the growth of bigger crystals. The rate of growth depends on the size of the crystals. This phenomenon narrows or "focuses" the size distribution of the NCs (Peng *et al.* 1998). When the reagents get used up in the reaction, the critical size becomes larger than the average size of NCs. Therefore, the distribution broadens, because some smaller NCs start dissolving and larger ones keep growing. This is Ostwald ripening, or defocusing of size distribution. Refocusing can occur by injecting additional reagents at the growth temperature, which brings back the critical size to a smaller value. Therefore, critical size is directly proportional to the concentration of reagents. Higher solution temperatures can also enhance Ostwald ripening, leading to larger average NC size with a compensating decrease in nanocrystal number (Ratke and Voorhees 2002). This process is represented as a flowchart in Figure 2.4.

Size of NCs also depends on the ratio of the concentration of reagents to that of surfactants. Lower ratio can produce smaller nuclei and thus smaller size NCs (Sun *et al.* 1999). The chemistry of surfactants also plays a role in controlling the NC size. If a surfactant binds tightly to the NC, then it can hinder the growth and vice versa. Alternatively, the size of NCs may also be increased by adding more reagents, as long as the rate of material addition and temperature is controlled.

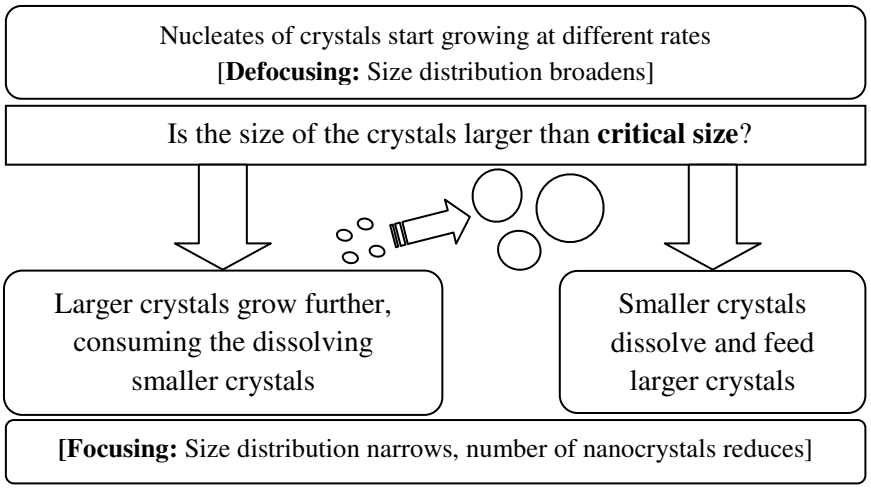

Figure 2.4: Flowchart describing the Ostwald ripening process in a chemical reaction

When the NC sample reaches the desired size, quenching can arrest further growth. The NC dispersion is stable if the interaction between the capping groups and the solvent is favorable, providing an energetic barrier to counteract the van der Waal's attractions between NCs.

The synthesis of NCs is primarily based on collisions between molecules, which is the case with all the chemical reactions. These collisions occur soon after decomposition of the reagents, resulting in nucleation. The growth, size, and properties of NCs can be controlled by adjusting temperature, growth time, concentration of reactants and surfactants, and the concentration ratio of reagents to surfactants. NC size increases with

increasing reaction time, as more material adds to NC surfaces, and with increasing temperature, as the rate of addition of material to the existing nuclei increases.

2.2. Role of shell in core/shell nanocrystals

The trap sites present in the crystal that can acquire carriers from the activator levels considerably affect the efficiency of the radiative transitions between the energy levels of the luminescent ions. If the luminescent centers are close to the surface, the excited carriers in their energy levels may get trapped by the trap levels created due to the organic layer or the surface defect. This can lead to a non-radiative recombination, thereby reducing the luminescence efficiency. An effective strategy to improve the efficiency is to make core/shell structures (Stouwdam and van Veggel 2002). As shown in Figure 2.5, the shell tends to passivate the surface traps. Recently, Stouwdam *et al.* reported the synthesis of lanthanum fluoride core/shell nanoparticles doped with luminescent lanthanide ions emitting in the visible or near infrared with a significantly higher PL intensity than the core sample (van Veggel and Stouwdam 2004).

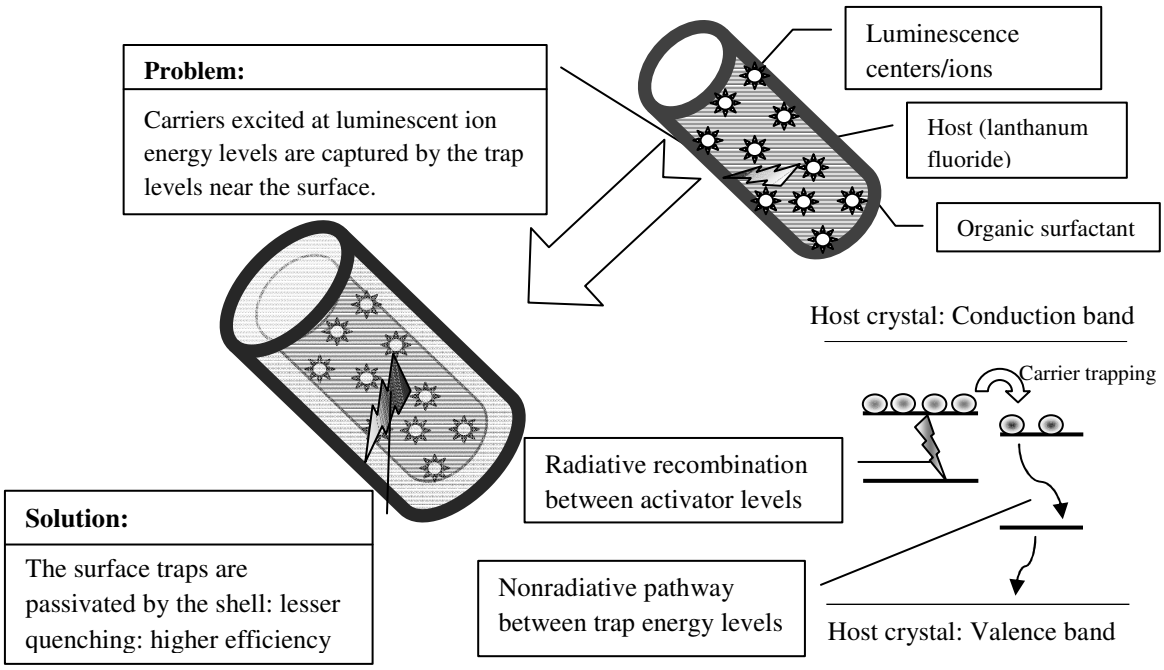

Figure 2.5: Core/shell structure passivates surface traps

Core/shell structures are also needed when the core material is unstable, as is the case for the hygroscopic lanthanum bromide. The shell serves as a protective coating, thereby making the core/shell nanocrystals stable.

2.3 Structural and compositional characterization

Transmission electron spectroscopy and energy dispersion spectroscopy were used to structurally and compositionally characterize various synthesized NCs. TEM images are extremely valuable in the structural characterization of nanocrystals, due to their high resolving capacity and magnification power.

2.3.1 The TEM microscope

A transmission electron microscope uses electrons to create an image. It has much higher magnification than the optical microscope (about 2 million times) and can reach atomic level resolution. A major limitation of visible light microscopy is that the resolution is limited by the wavelength of light. For example, no object smaller than 500 nm in size can be resolved using a green (500 nm) light source. Ultraviolet light can be used, but it soon runs into the problem of absorption. Like all matter, electrons have both wave and particle properties. As described by Heisenberg's principle, an electron beam can in some circumstances be made to behave like a beam of electromagnetic radiation. The wavelength of this radiation is dependent on the energy of the electron, according to de Broglie's principle. Therefore, by adjusting the accelerating fields of the electron emission gun, the wavelength can be tuned to the order of angstroms, which is much lower than the wavelength of optical radiation. These electrons interact with the sample by electrical charge, which results in an image from the interactions. In simple terms, a TEM microscope uses beams of high-energy electrons that have extremely small wavelengths and therefore can achieve much higher spatial resolution.

Transmission electron microscopy (TEM) is an imaging technique in which a beam of high energy electrons are transmitted through a specimen, an image is formed, magnified, and directed to appear on a fluorescent screen or detected by a sensor such as a CCD camera. TEM is widely used in bio-medical and material sciences fields for structural characterization of extremely small particles. The specimen or the sample must be very thin and must be capable of withstanding the high vacuum in the system. An electron source emits a beam of high-energy electrons. Instead of glass lenses focusing the light in

the light microscope, the TEM uses electromagnetic lenses to focus the electrons into a narrow beam. The electron beam then travels through the specimen under study. Depending on the density of the material present, some of the electrons are scattered and disappear from the beam. At the bottom of the microscope the unscattered electrons hit a fluorescent screen, which gives rise to a "shadow image" of the specimen with its different parts displayed in varied shades of grey according to their density. In contrast to light imaging, a crystalline material interacts with an electron by diffraction and not by absorption. The intensity of this diffraction depends upon the orientation of the atomic planes in the crystal relative to the electron beam. From the diffraction pattern obtained, the crystal structure can be studied.

In this work, the JEOL 2010 High-Resolution TEM microscope system was used in conjunction with a sensitive Oxford Instruments X-Ray detector and an energy loss spectrometer for energy dispersive spectroscopy. The microscope could achieve at most 0.14 nm spatial resolution with about 1 million times magnification capability. The system operated at an accelerating voltage of 200 kV and about 6 picoamps of operating current could be achieved.

2.3.2 Sample preparation and measurement setup

The TEM sample grid is a unique device in itself that helps to create thin layers of samples from colloidal dispersions. The grid is made up of a copper mesh supported by a thin carbon film. The mesh forms roughly about 200 square grid slots (Figure 2.6) backed by the film. In general, the TEM sample was prepared by placing a small drop of the nanocrystal colloidal dispersion on the grid, allowing the continuous medium to evaporate and the nanoparticles to settle down on the carbon film into the grid slots.

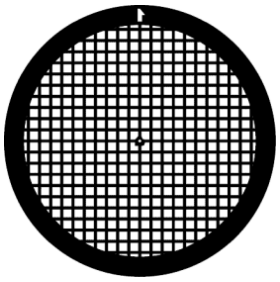

Figure 2.6: Typical TEM grid: 200 mesh copper grid on carbon film

However, this conventional method produced highly disordered and non-uniform distributions on the grid, which was unfavorable for high-resolution imaging. Therefore, an improved sample preparation method was adopted from (Murray *et al.* 2001), in which, a combination of solvent and non-solvents is used to prepare uniform nanocrystal superlattices. In this method, first a drop of non-solvent to the nanoparticles was placed on the grid followed by a drop of the NC dispersion in its solvent. This allows the nanoparticles to separate from each other while settling down on the grid thereby producing uniformly spaced particle arrangements (Murray *et al.* 2001). Due to shape constraints of the cerium-doped lanthanum halide nanoparticles, a perfect superlattice arrangement could not be obtained. However a better, more uniform distribution was obtained compared to the conventional sample preparation technique.

2.4 Optical characterization

Optical characterization basically refers to the determination of optical characteristics of the sample both quantitatively and qualitatively, and identification with a material or material system of known characteristics. In this case, optical characteristics include photoluminescence emission and excitation spectra, absorption spectrum, luminescence decay lifetime measurement and quantum efficiency measurement. All samples were characterized within a period of a week from the time of synthesis. One of the most

important and standard optical characterizations needed for an optically active sample is the determination of photoluminescence spectra. When a sample is subject to an electromagnetic radiation of energy sufficient to excite an electron from the valence band (ground state) of the atom of the material, the electron is excited from a lower energy level to a higher energy level. In simple terms, an electron is excited and an electron-hole pair is said to be formed when an electron acquires enough energy to leave the electrostatic hold of the nucleus but still lives in the vicinity of the atom controlled by the periodic potential or wave function of the crystal. The vacancy created in the atom is known as a hole in the virtual sense. Therefore, eventually when the excited electron loses energy in one of the many available mechanisms, it relaxes back into the vacancy (hole) present in the atom. Now, when the release of energy occurs in the form of photons (light) instead of phonons (heat), it is considered as a useful relaxation process (radiative recombination) known as photoluminescence. Fluorescence and phosphorescence are the two major light emission mechanisms classified under photoluminescence. Fluorescence is the property of some atoms and molecules to absorb light at a particular wavelength and to subsequently emit light (usually at a longer wavelength) after a brief interval known as fluorescence lifetime (on the order of nanoseconds). The process of phosphorescence occurs in a manner similar to fluorescence, but with a much longer excited state lifetime (on the order of microseconds).

Born in Ukraine in 1898, Alexander Jablonski is best known as the father of fluorescence spectroscopy. Jablonski's primary scientific interest was the polarization of photoluminescence in solutions, and in order to explain experimental evidence gained in the field, he differentiated the transition moments between absorption and emission. His

work resulted in his introduction of what is now known as a Jablonski Energy Diagram, shown in Figure 2.7 (Davidson 2003).

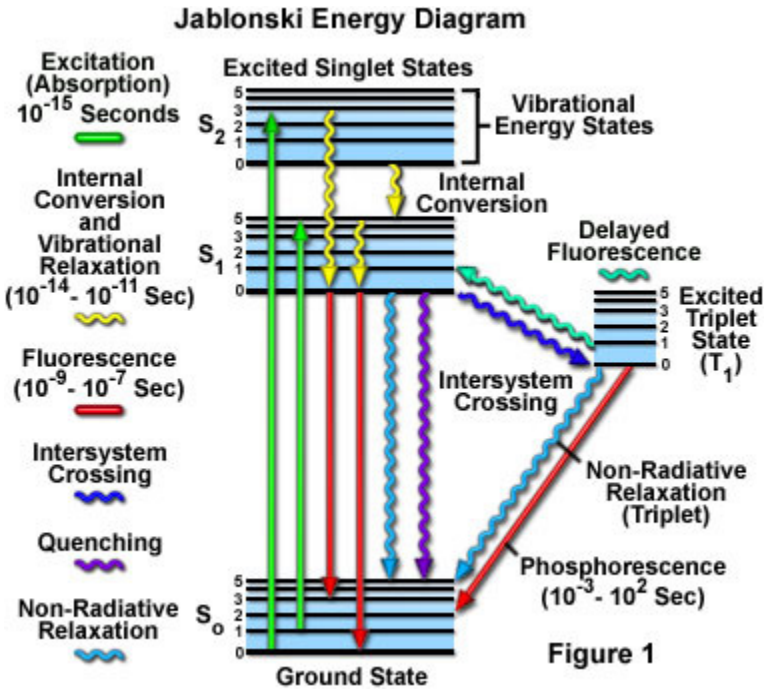

Figure 2.7: Jablonski energy diagram (Davidson 2003)

Inferring from this diagram, it is expected to observe a Gaussian-like distribution in both the photoluminescence and absorption spectra, since there is a band of states in the ground state and the excited state between which any possible transition can occur, as long as enough energy is provided for the transition.

From the absorption spectrum of a sample it is possible to determine the bandgap of the material and also discrete excited state energy level positions. It is possible to accurately determine the most favorable emission transition from the photoluminescence emission spectrum that can be eventually used to characterize an unknown material from the known values of characteristic emission wavelength of materials. In addition to this, change in the position of the quantized energy states, as an effect of certain treatments on

the sample (like shell growth, annealing, etc.) can be determined from observing the variation in intensity and/or wavelength of the photoluminescence spectra of the material that can again be used to indirectly evaluate such treatments on the sample. Further, luminescence decay time or lifetime measurements can provide data to discern between various components of emission in terms of lifetimes. From such knowledge it is possible to determine the fraction of radiative and non-radiate emission components.

2.4.1 Absorption measurement setup

Most absorption measurements were performed using the Thermo Scientific NanoDrop™ 1000 UV-vis spectrophotometer, except for the absorption measurements of the chitosan-capped lanthanum fluoride NCs, which were performed using the Cary™ 300 UV-vis spectrophotometer. In general, a UV-vis spectrophotometer consists of a light source emitting both in the UV and visible spectral range, an excitation monochromator, and a photodetector connected to a data acquisition (DAQ) system, as shown schematically in Figure 2.8. In this case, the detector is placed right behind the sample, such that the light from the excitation source traverses a path length through the sample and the unabsorbed (transmitted) light is detected by the photodetector.

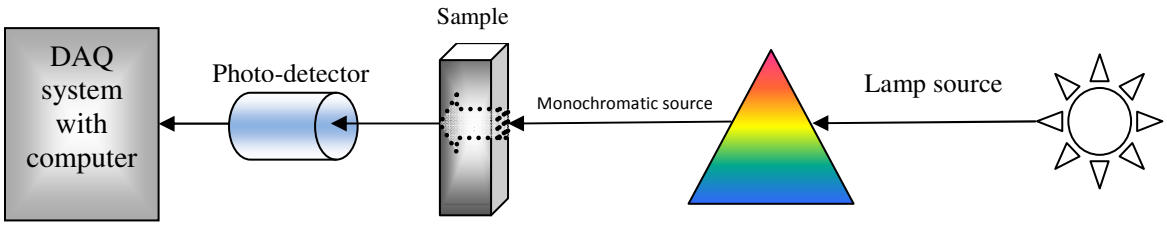

Figure 2.8: Absorption measurement setup

In a dual-beam spectrophotometer such as Cary™ 300, the inverse of the detected spectrum subtracted from the baseline (a cuvette filled with solvent) gives the absorbance

spectrum of the dispersed NCs in the sample. For short-wavelength UV excitation, quantitative absorbance measurements become increasingly difficult due to the fact that most of the solvents start absorbing strongly in the UV. Therefore, careful calibration is essential when measuring absorbance of UV-excited samples. Since the NCs absorb in UV wavelengths, special 5 mL cuvettes, made of a UV-transparent quartz-based material, marketed as Spectrosil®, were used to hold the samples and the solvents.

2.4.2 Photoluminescence excitation, emission, and lifetime measurement setup

A typical setup for photoluminescence measurement (shown in Figure 2.9) includes a light source, which is usually a lamp source or a laser source in some cases. A monochromator is required in order to selectively allow only a narrow band of the excitation spectrum through to the sample and emission spectrum through to the detector. This is important to be able to scan a range of wavelengths for emission with a particular resolution while the sample is excited at a specific excitation wavelength.

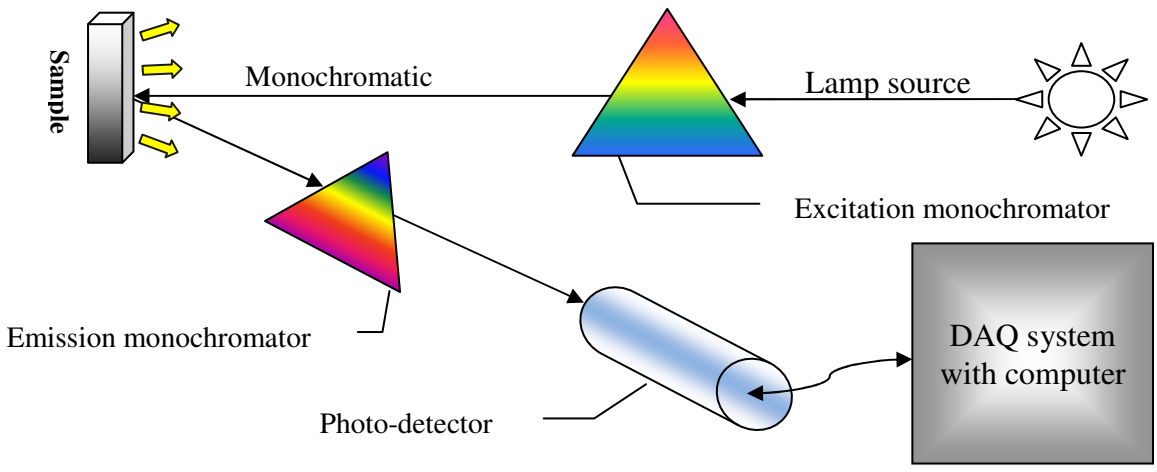

Figure 2.9: Photoluminescence spectra measurement setup (front facet detection)

A detector that can usually detect both ultraviolet and visible wavelengths (200-800 nm) with a fairly flat response is required in conjunction with a data acquisition (DAQ) system that can record and print the spectra.

The PLE (photoluminescence excitation) and PL emission measurement setup used in this work was Horiba Jobin Yvon Fluorolog-3 Spectrofluorometer®, with a broadband 450-W ozone-free Xe source, double Czerny Turner excitation spectrometer, single Czerny Turner emission spectrometer, and reflective optics. The instrument was equipped with a room-temperature multialkali PMT emission detector R928P (180 nm - 850 nm range), TE cooled NIR-PMT module H9170-75 (950 nm - 1700 nm range) for steady-state measurements, and a data acquisition system connected to the computer. Emission detector electronics employing photon-counting for low-light-level detection was capable of detecting 50-femtomolar fluorescein.

With the help of an integrating sphere coated with a special reflective material, it was also possible to determine quantum efficiency of samples using this system. However, since the material used for coating had poor reflectance below 300 nm wavelengths, the system was incapable of measuring quantum efficiency of samples that required less than 300 nm excitation, which was the case for the NCs studied in this thesis.

Since both excitation and emission wavelengths for all the NCs fall in the UV spectral range, the UV-transparent Spectrosil® cuvettes were used to prepare samples for PL measurements. The cuvette was filled at least up to the $3/4^{th}$ level with the NC dispersion. To the best possible extent, the concentration of the sample, sample-level in cuvette, and

the temperature of the sample compartment were maintained constant to reduce systematic measurement errors.

2.4.3. Photoluminescence lifetime measurement setup

PL lifetimes were measured using a time-correlated single-photon counting (TCSPC) accessory on the Horiba Jobin Yvon Fluorolog-3 Spectrofluorometer®. A variety of pulsed diode lasers and LEDs (repetition rate up to 1 MHz) were available, emitting between 250 nm and 560 nm. Fluorescence lifetimes as short as ~100 ps could be measured by R928P detector assembly in the 300 nm to 850 nm spectral range. The fall-time (time to reach 10% of the peak PL emission intensity after the excitation was removed) was measured and a histogram was plotted. The data points in the histogram were fitted using a multi-exponential fit that provided the weighted decay-time components of the PL emission from the sample.

References

1. Brown, T. L., H. E. LeMay, and B. E. Bursten. "*Chemistry: The Central Science"* Tenth Edition, Upper Sadle River, NJ: Pearson Education Inc., 2006.
2. Davidson, M. W. "Science, optics & you" *Molecular expressions,* National High Magnetic Field Laboratory. August 1, 2003. http://micro.magnet.fsu.edu/optics/timeline/people/jablonski.html (accessed September 14, 2008).
3. Murray, C. B., S.H. Sun, W. Gaschler, H. Doyle, T. A. Betley, and C. R. Kagan. "Colloidal synthesis of nanocrystals and nanocrystal superlattices" *J. Res. & Dev.* (IBM) 45, no. 1 (2001): 256-279.

4. Murray, C. B., D. J. Norris, and M. G. Bawendi. "Synthesis and characterization of nearly monodisperse CdE (E = S, Se, Te) semiconductor nanocrystallites" *J. Am. Chem. Soc.* 115, No. 2 (1993): 1203-1211.
5. Peng, X. G., J. Wickham, and A. P. Alivisatos. "Kinetics of II-VI and III-V colloidal semiconductor nanocrystal growth: "Focusing" of size distributions" *J. Am. Chem. Soc.* 120, no. 21 (1998): 5343-5344.
6. Ratke, L., and P. W. Voorhees. "*Growth and Coarsening: Ostwald Ripening in Material Processing"* Springer, 2002.
7. Stouwdam, J. W., and F. C. J. M. van Veggel. "Near-infrared emission of redispersible Er^{3+}, Nd^{3+}, and Ho^{3+} doped LaF_3 nanoparticles" *Nano Letters* 2, no. 7 (2002): 733-737.
8. Sun, S., C. B. Murray, and H. Doyle. "Controlled assembly of monodisperse e-cobalt-based nanocrystals" *Mater. Res. Soc. Symp. Proc.* 17, no. 5, (1999), 385-398.
9. Van Veggel, F. C. J. M., and J. W. Stouwdam. "Improvement in the luminescence properties and processability of LaF_3/Ln and $LaPO_4$/Ln nanoparticles by surface modification" *Langmuir* 20, no. 26 (2004): 11763-11771.
10. Vengrenovich, R. D., Yu. V. Gudyma, and S. V. Yarema. "Ostwald ripening of quantum-dot nanostructures" *Semiconductors* 35, no. 12 (2001): 937-945.
11. Wang, F., Y. Zhang, X. P. Fan, and M. Q. Wang. "One-pot synthesis of chitosan/LaF_3:Eu^{3+} nanocrystals for bio-applications" *Nanotechnology* 17, no. 6 (2006): 1527-1532.

Chapter 3

Synthesis and characterization of chitosan-capped cerium-doped lanthanum fluoride colloidal nanocrystals

3.1. Synthesis of chitosan-capped cerium-doped lanthanum fluoride colloidal nanocrystals in aqueous medium

As early as in 1990, Moses and Derenzo first reported the scintillating properties of bulk cerium-doped lanthanum fluoride heavy atom scintillator (Moses and Derenzo 1990). The colorless, odorless, non-hygroscopic crystals were grown using vertical Bridgeman technique, cut and polished subsequently. Since then, there have been several publications on bulk lanthanide-doped lanthanum fluoride (Rodnyi *et al*. 1995), (Dorenbos 2000), (Derenzo 2005). This section reports on the synthesis of highly-luminescent chitosan-capped cerium-doped lanthanum fluoride colloidal NCs. The optical and structural properties of cerium-doped lanthanum fluoride synthesized as colloidal nanocrystals have not been reported prior to this work.

In addition to being a prospective good scintillator material, lanthanide-doped nanocrystals have also shown high promise recently as biological fluorophores based on some of the arguments given by Wang and coworkers (Wang *et al.* 2006). They usually possess good chemical stability and resist photobleaching. Their toxicity is mostly low and, therefore, they can be used *in vivo* for biomedical applications. Importantly, the optical properties of such lanthanide-doped nanocrystals are independent of particle size and can be tuned by doping with suitable lanthanide ions that emit at their own

characteristic wavelengths (Wang *et al*. 2006). However, for the fluorophores to be usable *in vivo*, the nanocrystals need to be hydrophilic. The surface molecules or the end ligands must be hydrophilic in nature. Furthermore, for conjugation with bio-molecules, the surface usually needs to be modified to contain specific functional groups. Therefore, for the lanthanide-doped nanocrystals to be best suitable for biological applications, the surface of the nanocrystals must be hydrophilic and bio-functional. Chitosan has been reported as a naturally occurring hydrophilic and bio-functional biopolymer (Miyazaki *et al.* 1981), (Gupta and Kumar 2000). It contains amino and hydroxyl groups that can be used to attach bio-molecules.

Adapted from the method described by Wang *et al.*, the following section details a straightforward one-pot colloidal approach to synthesize water-soluble cerium-doped lanthanum fluoride nanocrystals.

3.1.1. Basic chemical reaction

The following gives the balanced chemical reaction that is expected to occur at the nucleation phase of chitosan-capped $LaF_3:Ce^{3+}$ NCs:

$$1\ wt\%\ chitosan\ solution_{(aq)} + 2\ mmol\ (LaCl_3 + CeCl_3)_{(aq)} + 6\ mmol\ NH_4F_{(aq)} \xrightarrow{75^{\circ}C} 2\ mmol\ chitosan/LaF_3{:}Ce^{3+}\downarrow + 6\ mmol\ NH_4Cl_{(aq)}$$

3.1.2. Preparation of precursors

Lanthanum chloride hexahydrate 99.99%, cerium chloride heptahydrate 99.999%, ammonium fluoride 99.9%, medium molecular weight chitosan, and 2 M ammonia solution in methanol were purchased from Sigma Aldrich and used as such. 0.2 M stock solutions of lanthanum chloride and cerium chloride in DI water were prepared separately. A stock solution of 1 weight percentage chitosan in DI water at pH 2.0 was

prepared by addition of few drops of 37% hydrochloric acid. Also, a 0.6 M ammonium fluoride solution in DI water was prepared. All stock solutions were prepared in quantities approximately equal to the requirement and used in the subsequent synthesis.

3.1.3. Synthesis procedure

For the synthesis, the Schlenk-line setup was used so that the entire reaction could take place in an inert argon atmosphere, as explained in Section 2.1.1. Lanthanum fluoride nanocrystals were synthesized through a simple co-preciptation method following Wang *et al.* with slight modifications. In order to synthesize lanthanum fluoride NCs doped with 5% cerium, 9.5 mL of 0.2 M lanthanum chloride solution and 0.5 ml (5% of 10 mL) of 0.2 M cerium chloride solution were added to a three-neck round-bottom borosilicate flask containing 25 mL of 1 wt% chitosan solution. The lanthanide precursor solution in chitosan was stirred at 600 rpm under argon atmosphere. Then, 10 mL of 0.6 M ammonium fluoride solution was added to the flask using a syringe, under constant stirring (600 rpm). As nucleation started to occur, the precipitation of lanthanum fluoride was observed, with the solution turning milky. In order to precipitate the excess chitosan and to neutralize the pH of the solution to 6.5, dilute ammonia solution was added drop-wise to the flask. Subsequently, the mixture in the flask was heated to 75 $^{\circ}$C and kept at that temperature for 2 hours, while stirring under argon atmosphere. The precipitated nanocrystals were collected by centrifugation and washed several times with DI water and 0.5% acetic acid solution in order to remove the un-reacted reagents and by-products. The final precipitate was dispersed and stored in DI-water at room temperature. Multiple syntheses were performed using the same procedure and a high degree of repeatability was observed with the sample

characteristics. When stored at normal concentrations, the sample was viscous and milky in appearance.

3.2. Structural characterization

The low-resolution and high-resolution TEM images of chitosan-capped, cerium-doped lanthanum fluoride colloidal NCs are given in Figure 3.1 in increasing order of magnification.

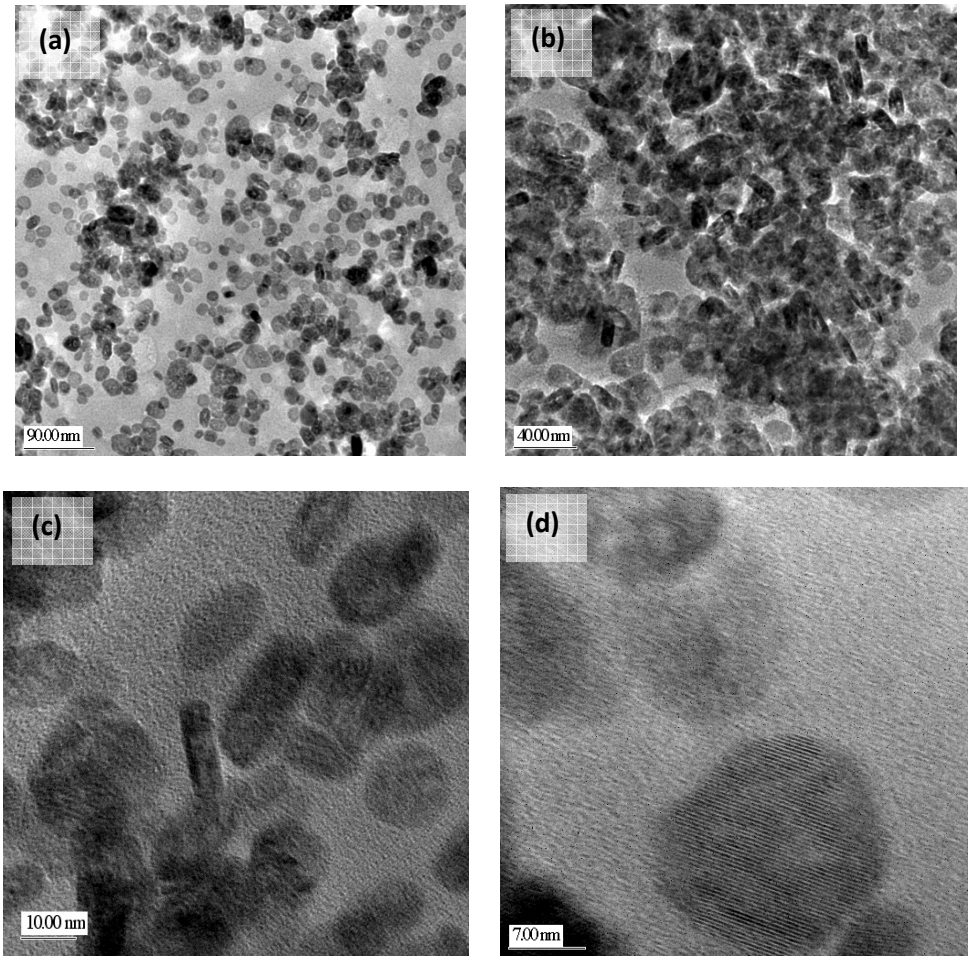

Figure 3.1: (a) and (b) Low-resolution TEM images of chitosan- capped 5% cerium-doped lanthanum fluoride NCs with 90 and 40 nm scale bars, respectively, (c) and (d) High-resolution TEM images of the NCs with 10 and 7 nm scale bars, respectively

The TEM images show hexagonal platelets oriented both flat and side-on. The mean size of the particles was 16.5 nm with a standard deviation of 25% (measured from a sample of 50 particles from different images). Since there were more rod-like shapes when the particles were closely packed, as seen in image 3.3(b), and more disc-like shapes when the particles were loosely packed, as seen in image 3.3(a), it was inferred that both shapes corresponded to the same hexagonal platelet-like nanoparticles, some oriented side-on and some flat. High-resolution image 3.3(d) shows the hexagonal structure of the nanocrystal, which confirms to the reported crystal structure of bulk lanthanum fluoride (Stubicar *et al.* 2005). The image also shows the crystal lattice planes clearly. The fringe separation measured from this image is about 3.5 angstroms, which is believed to be one of the three lattice constants of the hexagonal crystal structure. This value agrees closely with the reported lattice constant of 3.23 angstroms derived from X-ray diffraction (XRD) data obtained from lanthanum fluoride nanocrystals (Yanesa *et al.* 2007). This leads to a conclusion that the nanocrystals are hexagonal single crystals of lanthanum fluoride.

To get the energy dispersion spectrum (EDS) data, the electron beam was focused on a single NC and the peaks were identified using the Oxford Instruments ISIS software. Data obtained from multiple single-NC measurements showed good repeatability.

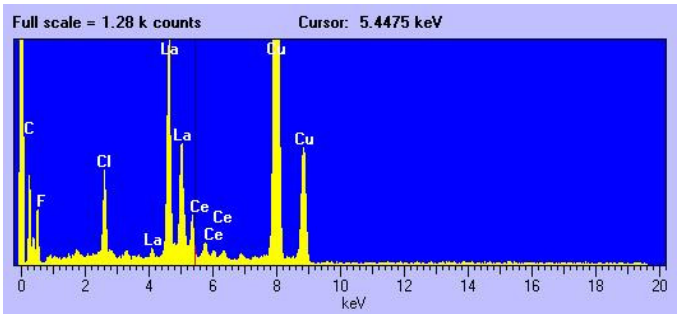

Figure 3.2: Energy dispersion spectrum of chitosan-capped lanthanum fluoride NCs doped with 5% cerium

The EDS spectrum in Figure 3.2 confirms the presence of cerium, lanthanum, and fluorine in the nanoparticles. The spectrum also shows the presence of chlorine, which may be due to the residue of some ammonium chloride or lanthanum chloride in the sample. Quantitative elemental analysis could not be performed due to software limitations.

3.3. Optical characterization

The cerium-doped lanthanum fluoride/chitosan water-soluble nanocrystals were synthesized and stored as a colloidal dispersion in DI water. In appearance, the sample was viscous in nature and white, milky, and translucent in appearance (Figure 3.3).

Figure 3.3: Appearance of chitosan-capped LaF_3: $Ce3^+$ NCs immediately after synthesis

As the first step in optical characterization, absorption spectra of the samples were determined using the spectrophotometer. A sample of the NC colloidal dispersion was taken in a UV-transparent cuvette along with another sample of the solvent itself (which is DI-water in this case) in a similar cuvette for subtracting the background absorption.

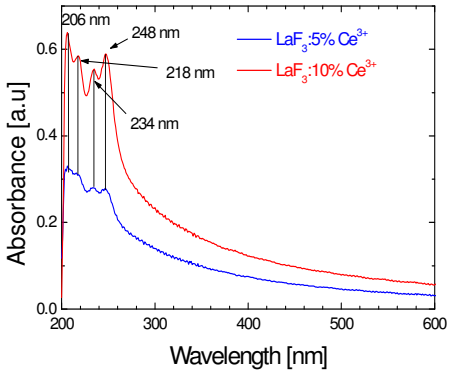

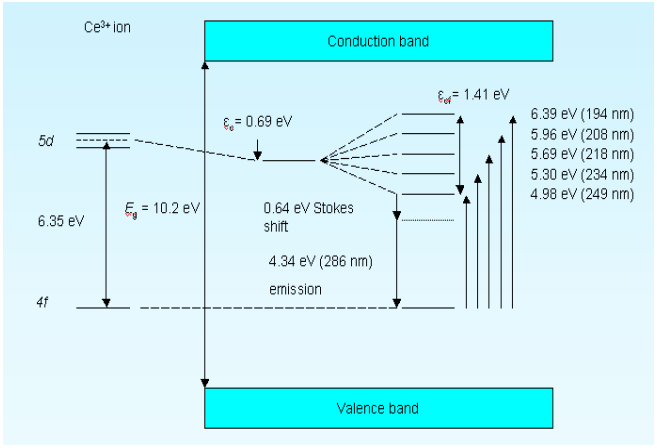

Figure 3.4: The multiple peaks in 10% cerium-doped lanthanum fluoride absorption spectra agrees exactly with the internal energy level configuration of cerium ion doped into a lanthanum fluoride host lattice (Dorenbos 2000)

The absorption spectra for chitosan-capped lanthanum fluoride nanocrystals doped with 5% and 10% cerium are shown in Figure 3.4. The spectrum from LaF_3 NCs doped with 10% cerium shows four distinct, clearly resolved peaks. Since the absorption coefficient depends on the unknown concentration of the sample, it could not be extracted from these data.

The excitation spectrum was recorded for the 5% cerium-doped LaF_3 NCs sample by scanning the excitation wavelength from 200 nm to 290 nm, while the emission monochromator was fixed at 312 nm. The excitation PL curve was corrected for the nonuniformity of the lamp intensity spectrum.

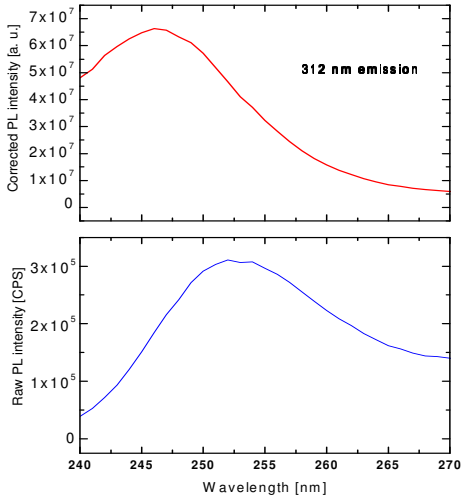

Figure 3.5: PL excitation spectra of lanthanum fluoride/ chitosan colloidal NCs doped with 5% cerium

The optimum excitation was determined to be 247 nm from the corrected PL excitation spectrum shown in Figure 3.5. This closely agrees with the position of lower energy levels in the 5d to 4f configuration of cerium, confirming excitation of the cerium ions.

For PL emission measurements, the excitation monochromator was configured to pass 247 nm light with a 1 nm spectral resolution and the emission monochromator was set to scan from 280 nm to 540 nm with a similar spectral resolution of 1 nm. The emission was detected from the front facet of the cuvette, which minimized absorption and scattering effects. The NC emission spectrum was compared with the emission obtained from the cerium chloride precursor solution prepared at the synthesis concentration to eliminate the possibility of free cerium ion emission. The emission spectra of LaF_3: 5% Ce^{3+} NCs and cerium chloride precursor solution in water are shown in Figure 3.6. The analysis of cerium emission in lanthanum fluoride is given in more detail in Section 3.4.

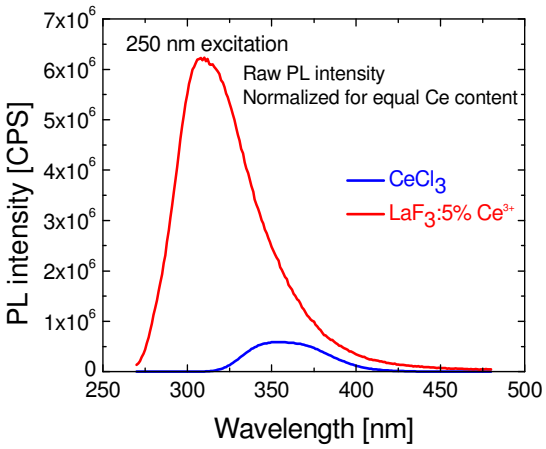

Figure 3.6: PL emission spectrum of lanthanum fluoride/chitosan colloidal NCs doped with 5% cerium in comparison with that of the cerium chloride precursor solution at 250 nm excitation

The PL emission spectrum in Figure 3.6 shows a clearly defined emission peak at 312 nm. The curve is fairly narrow with a full-width-at-half-maximum (FWHM) of 48 nm.

The rising edge is steeper than the falling edge. The emission was highly intense with about 1.5 million counts per second recorded at the peak wavelength, clearly distinguished and red shifted from the broad low intensity peak of the cerium precursor solution (free cerium ions). This leads to the preliminary inference that the emission is originating from the cerium ions incorporated in the lanthanum fluoride lattice. Although it is expected that increase in cerium concentration must lead to increase in PL emission intensity, it is suspected that an optimum exists in the cerium doping concentration due to possibility of emission quenching at high cerium concentrations. This determination of optimum cerium concentration is dealt with in detail in Chapter 5 of this thesis.

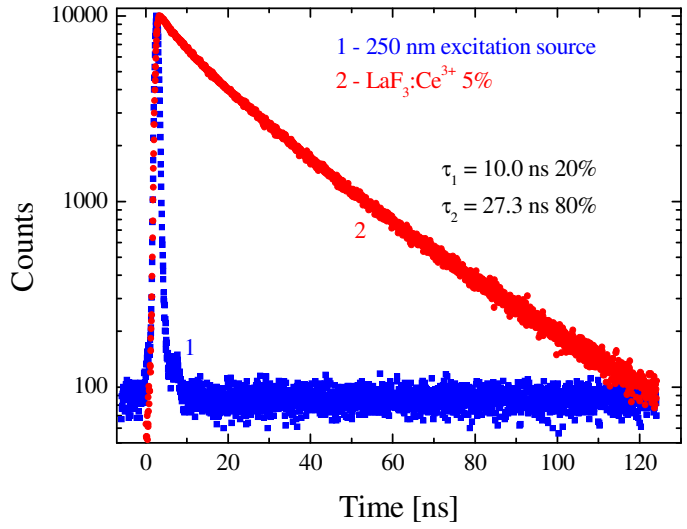

Figure 3.7: PL decay plot for lanthanum fluoride/chitosan NCs doped with 5% cerium

The PL emission lifetime or the decay time was measured using a fast sub-nanosecond pulse source included with the spectrofluorometer system. The obtained PL decay data shown in Figure 3.7 were fitted using a multi exponential fit to separate out the different lifetimes. The PL decay plot shows 20 percent of 10 ns short component and

80 percent of the 27.3 ns long component. Moses and Derenzo reported 3 ns (10%) and 26.5 ns (86%) decay components for bulk lanthanum fluoride crystals doped with 10% cerium (Moses and Derenzo 1990).

3.4. Analysis of cerium emission

The luminescence of the trivalent lanthanide ions arises either from intraconfigurational $4f^n \rightarrow 4f^n$ transitions within the 4*f* shell (Eu^{3+}, Er^{3+}), or from interconfigurational $5d^1 4f^{n-1} \rightarrow 4f^n$ transitions (Ce^{3+}, Pr^{3+}) between 5*d* and 4*f* shells. These excited states can be very efficiently quenched in the presence of the high-energy vibrations of organic solvents, polymers, or ligands. Doping of the lanthanide ion into LaX_3 (X = Cl, F, Br, I) materials provides strong shielding of the 4*f* and 5*d* electrons from the environment. The 5*d* electron states, however, turn out to be very sensitive to the local environment of the host material. In particular, a profound influence of the halide anions on the energy of the 5*d* levels of Ce^{3+} in LaX_3 (X = Cl, Br, I) has been reported (van Loef *et al*. 2003). As a result, emission from the lowest-energy state deriving from the $5d^1$ electron configuration in Ce^{3+} is observed as a broad peak, ranging from 535 nm in YAG: $Ce3^+$ to 286 nm in LaF_3: $Ce3^+$ (Dorenbos 2000).

The combination of the multiple absorption peaks between 200 nm to 250 nm, the excitation peak at 253 nm, and the emission peak at 312 nm clearly are characteristic of the 5d → 4f emission expected from the cerium ions (Coutts and McGonigle 2004). The free-ion configuration of cerium consists of xenon like core with 54 electrons and a valence shell containing one 4f electron. This is further split into two $^2F_{7/2}$ and $^2F_{5/2}$ spin levels. The excited 5d levels are also split into the $^2D_{3/2}$ and $^2D_{5/2}$ energy levels due to

spin-orbit interactions. However when the cerium ions are embedded in a host matrix, the energy level configuration changes considerably. The three distinct absorption peaks are believed to be due to the quantum confined Stark effect that tends to split the excited 5d levels in cerium into 4 to 5 separate energy levels (Dorenbos 2000), (Henderson and Bartram 2000). The decay scatter can be described as the sum of two exponentials, a short lifetime component at 10 ns and another one at 27 ns. The measured short lifetime of the sample is due to the fact that the 5d → 4f transition in cerium is electrical dipole allowed (Aull and Jenssen 1986), (Coutts and McGonigle 2004). The presence of the fast component in the lifetime confirms the presence of chitosan capping that effectively prevents the quenching of the fast emission. The incorporation of cerium ions in the lanthanum fluoride lattice is established by the multiple absorption peaks between 200-250 nm and the narrow 312 nm emission peak characteristic of the 5d → 4f cerium emission. For Ce^{3+} in an octahedral complex, two parameters are of interest in determining the absorption spectra. First, the center of gravity in a 5d configuration is lower in a polarizable matrix than in the free-ion configuration. Second, the 5d level is split into multiple levels due to the crystal field (Aull and Jenssen 1986).

3.5. Summary

The excitation PL and the multiple peaks in the absorption spectra confirm the excitation of carriers from the lowest 4f level to the multiple 5d levels split by the electric field of the lanthanum fluoride crystal. The NCs also have a characteristic short PL lifetime similar to bulk $LaF_3:Ce^{3+}$ crystals. Additionally, the water solubility of the nanocrystal dispersion confirms the successful capping of the hydrophilic chitosan

molecules on the nanocrystals. In summary, inferring from the TEM, EDS, absorption, and PL results, the synthesis of chitosan-capped cerium-doped lanthanum fluoride colloidal NCs was successful.

References

1. Aull, B. F., and H. P. Jenssen. "Impact of ion-host interactions on the 5d-to-4f spectra of lanthanide rare-earth-metal ions. A phenomenonological crystal-field model" *Physical Review B* 34, no. 10 (1986): 1037-1044.

2. Coutts, D. W., and A. J. S McGonigle. "Cerium-doped fluoride lasers" *IEEE Journal of Quantum Electronics* 40, no. 10 (2004): 1430-1440.

3. Derenzo, S. E. "Who needs better nuclear detector materials and how do we find them?" *Interdisciplinary Instrumentation Colloquium.* Berkeley: Ernest Orlando Lawrence Berkeley National Laboratory, (2005).

4. Dorenbos, P. "5d level energies of Ce^{3+} and the crystalline environment" *Phys. Rev. B* 62, no. 5 (2000): 15640-15649.

5. Gupta, K. C., and M. N. V. R. Kumar. "An overview on chitin and chitosan applications with an emphasis on controlled drug release formulations" *Journal of Macromolecular Science; C Reviews in Macromolecular Chemistry and Physics* 40, no. 4 (2000): 273-308.

6. Henderson, B., and R. H. Bartram. *Crystal-Field Engineering of Solid-State Laser Materials* Cambridge: Cambridge Univ. Press, (2000).

7. Miyazaki, S., K. Ishii, and T. Nadai. "The use of chitin and chitosan as drug carriers" *Chem Pharm Bull* 3, no. 10 (1981): 3067-3069.

8. Moses, W. W., and S. E. Derenzo. "The scintillation properties of cerium-doped lanthanum fluoride" *Nuclear Instruments and Methods in Physics Research* A 299 (1990): 51-56.

9. Rodnyi, P., E. Melchakov, N. Zakharov, I. Munro, and A. and Hopkirk. "Fast luminescence of cerium-doped lanthanum fluoride" *Journal of Luminescence* 65, no. 2 (1995): 85-89.

10. Stubicar, N., p. Zipper, and B. Cherney. "Variety of aggregation and growth processes of lanthanum fluoride as a function of La/F activity ratio" *Crystal Growth & Design* 5, no. 1 (2005): 123-128.

11. van Loef, E. V. D., P. Dorenbos, C. W. E. van Eijk, K. W. Kramer, and H. U. Gudel. "Influence of the anion on the spectroscopy and scintillation mechanism in pure and Ce^{3+}-doped K_2LaX_5 and LaX_3 (X = Cl, Br, I)" *Phys. Rev. B* 68, no. 4 (2003): 45108.

12. van Veggel, F. C. J. M., and J. W. Stouwdam. "Improvement in the luminescence properties and processability of LaF_3/Ln and $LaPO_4$/Ln nanoparticles by surface modification" *Langmuir* 20, no. 26 (2004): 11763-11771.

13. Wang, F., Y. Zhang, X. P. Fan, and M. Q. Wang. "One-pot synthesis of chitosan/LaF_3:Eu^{3+} nanocrystals for bio-applications" *Nanotechnology* 17 (2006): 1527-1532.

14. Wang, Z., J. Bo, S. Song, L. Hu, J. Liu, and X. Zhen. "One-step synthesis of highly water-soluble LaF_3:Ln^{3+} nanocrystals in methanol without using any ligands" *Nanotechnology* 18, no. 46 (2007): 465-472

15. Yanesa, A. C., J. Del-Castilloa, J. Méndez-Ramosb, V.D. Rodríguezb, M.E. Torresa, and J. Arbiolc. "Luminescence and structural characterization of transparent nanostructured Eu^{3+}-doped LaF_3–SiO_2 glass–ceramics prepared by sol–gel method" *Optical Materials* 29, no. 8 (2007): 999-1003.

Chapter 4

Synthesis and characterization of anhydrously synthesized cerium-doped lanthanum fluoride core and core/shell colloidal nanocrystals

4.1. Anhydrous synthesis of cerium-doped lanthanum fluoride colloidal nanocrystals in methanol

The objective of creating a water-free synthesis route that would be compatible with the synthesis of cerium-doped lanthanum bromide NCs formed the motivation for the anhydrous synthesis of cerium-doped lanthanum fluoride colloidal nanocrystals. Adapted from Wang *et al.*, a completely water-free synthesis route was developed to synthesize cerium-doped lanthanum fluoride colloidal nanocrystals as described below (Wang *et al.* 2007).

4.1.1. Basic chemical reaction

The following gives the balanced chemical reaction that is expected to occur at the nucleation phase of cerium-doped lanthanum fluoride NCs anhydrously synthesized in methanol.

$$CH_3OH + 1\ mmol\ (La(NO_3)_3 + Ce(NO_3)_3) + 3\ mmol\ NH_4F \rightarrow 3\ mmol\ NH_4NO_3 + 1\ mmol\ \mathbf{LaF_3{:}Ce^{3+}/OH}$$

4.1.2. Preparation of precursors

Lanthanum nitrate hexahydrate 99.99%, cerium nitrate heptahydrate 99.999%, ammonium fluoride 99.9%, and anhydrous absolute methanol 99.9% were purchased

from Sigma Aldrich Co. and used as such. A 0.65 M lanthanide precursor solution was prepared by dissolving 1.3 mmol total (excessive amount) of lanthanum nitrate hexahydrate and cerium nitrate heptahydrate in 2 mL anhydrous methanol. The fluorine precursor solution was prepared by dissolving 3 mmol of ammonium fluoride in 35 mL anhydrous methanol in a three-neck round-bottom borosilicate flask. Ammonium fluoride, the fluorine precursor, was the limiting precursor in the reaction. In this reaction, methanol acts as a coordinating solvent that helps in hydrophilizing the NC surface by surface conjugation of hydroxyl groups.

4.1.3. Synthesis procedure

Due to the highly hygroscopic nature of anhydrous methanol and ammonium bromide, the entire precursor preparation process needed to be conducted in a controlled air-free environment. For this purpose, the argon-filled glovebox system was used, which provided an inert atmosphere to a high degree of purity (< 0.1 ppm H_2O and O_2) and controlled pressure.

For the synthesis, the sealed flask containing the fluoride precursor solution in anhydrous absolute methanol was attached to the Schlenk line to provide for a flowing argon atmosphere. The temperature of the flask was gradually raised to 60 $^{\circ}$C at the rate of 7 $^{\circ}$C / min. While the solution was stirring at 1000 rpm, the lanthanide precursor solution containing lanthanum nitrate and cerium nitrate at proportions corresponding to the required doping percentage was added to the flask with a single rapid injection, which instigated the nucleation process, as indicated by the appearance of white precipitate in the flask. To allow for the subsequent growth and ripening processes, the mixture in the

flask was stirred vigorously for two hours in argon atmosphere to produce the cerium-doped lanthanum fluoride core NCs.

The product was then purified by centrifugation at 5000 rpm with methanol. The final precipitate of cerium-doped lanthanum fluoride nanocrystals attached to hydroxyl groups was easily dispersible in DI water (due to the non-hygroscopic nature of lanthanum fluoride) to form a clear, transparent colloidal dispersion of nanocrystals, which was also observed to be stable without signs of flocculation or aggregation. Therefore, this synthesis proved to be far superior to the aqueous one, in terms of stability and optical transparency.

4.2. Anhydrous synthesis of cerium-doped lanthanum fluoride/undoped lanthanum fluoride core/shell colloidal nanocrystals

In an effort to produce core/shell nanocrystals of cerium-doped lanthanum fluoride, the similar anhydrous synthesis method adapted from (Wang *et al.* 2007) was combined with the core/shell method adapted from (van Veggel and Stouwdam 2004) and (DiMaio *et al.* 2008). The main motivation behind realizing core/shell nanocrystals was to prove the improvement in optical properties in a core/shell structure compared to the core and to prove the ability to successfully develop a stable undoped lanthanum fluoride shell. More specifically, a reduction in the quenching of the luminescence from the doped lanthanide ions (due to surface defects) and therefore higher PL intensity was expected as a result of adding the shell. The following synthesis procedure in anhydrous methanol presents a facile method to realize ligand-free hydrophilic core/shell nanocrystals.

4.2.1. Basic chemical reactions

The following gives the balanced chemical reactions that are expected to occur during the synthesis cerium-doped lanthanum fluoride/undoped lanthanum fluoride core shell NCs.

CH_3OH + 1 mmol ($La(NO_3)_3$ + $Ce(NO_3)_3$) + 3 mmol NH_4F → 3 mmol NH_4NO_3 + 1 mmol **$LaF_3:Ce^{3+}/OH$**

1 mmol $LaF_3:Ce^{3+}/OH$ + 4 mmol $La(NO_3)_3$ + 12 mmol NH_4F → 1 mmol **$LaF_3:Ce^{3+}$/ LaF_3/OH** + 12 mmol NH_4NO_3

4.2.2. Preparation of precursors

Lanthanum nitrate hexahydrate 99.99%, cerium nitrate heptahydrate 99.999%, ammonium fluoride 99.9%, and anhydrous absolute methanol 99.9% were purchased from Sigma Aldrich Co. and used as such. A 0.65 M lanthanide precursor solution was prepared by dissolving 1.3 mmol total (excess) of lanthanum nitrate hexahydrate and cerium nitrate heptahydrate in 2 mL anhydrous methanol. The fluoride precursor solution was prepared by dissolving 3 mmol of ammonium fluoride in 35 mL anhydrous methanol in a three neck round bottom borosilicate flask. The lanthanum precursor for the shell was prepared by dissolving 5.2 mmol lanthanum nitrate hexahydrate in 8 mL anhydrous methanol and the fluoride precursor for the shell was prepared similarly by dissolving 12 mmol ammonium fluoride in 8 mL anhydrous methanol.

4.2.3. Synthesis procedure

Due to the highly hygroscopic nature of anhydrous methanol and ammonium bromide, the entire precursor preparation process needed to be conducted in a controlled air free environment. For this purpose, a glovebox system was used that provides an inert atmosphere to a high degree of purity (< 0.1 ppm H_2O and O_2) and controlled pressure.

For the synthesis, the sealed flask containing the fluoride precursor solution in methanol was attached to the Schlenk-line to provide for a flowing argon atmosphere. The temperature of the flask was gradually raised to 60 $^{\circ}$C at the rate of 7 $^{\circ}$C / min. While the solution was stirring at 1000 rpm, the lanthanide precursor solution containing lanthanum nitrate and cerium nitrate at proportions corresponding to the required doping percentage was injected into the flask at one go which instigates the nucleation process indicated by the appearance of white precipitate in the flask. The mixture in the flask was stirred for 10 minutes followed by a drop wise alternating addition of the lanthanide and fluoride shell precursor solution. The gradual addition of shell precursors is believed to coat the existing cores as opposed to forming new nucleates as given by the growth conditions in the second chapter. After the shell injections, the mixture was allowed to stir for two hours while stirring at 800 rpm under flowing argon atmosphere.

The product was then washed by centrifugation at 5000 rpm with methanol. The final precipitate of cerium-doped lanthanum fluoride/undoped lanthanum fluoride core/shell NCs were again easily dispersible in DI water to form a clear, transparent colloidal dispersion of nanocrystals which was also observed to be stable without signs of flocculation or aggregation.

4.3. Structural characterization of anhydrously synthesized cerium-doped lanthanum fluoride and cerium-doped lanthanum fluoride/undoped lanthanum fluoride core/shell colloidal nanocrystals

TEM images of the cerium-doped lanthanum fluoride core-only NCs synthesized in anhydrous methanol were obtained. Figure 4.1 shows a series of low- and high-resolution bright-field TEM images of the core-only nanocrystals.

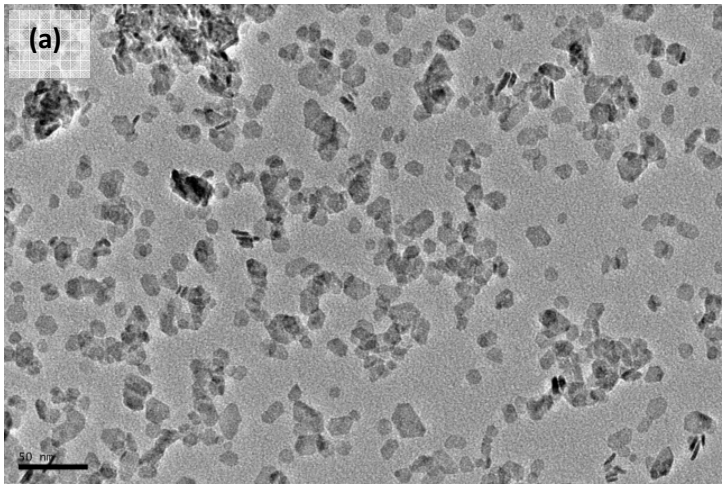

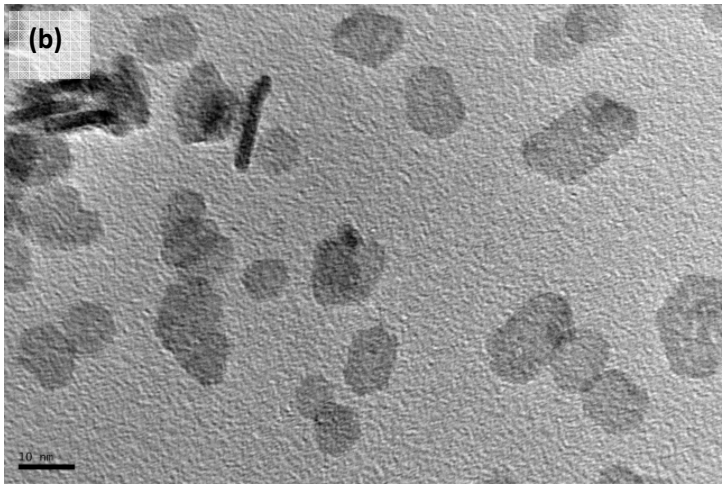

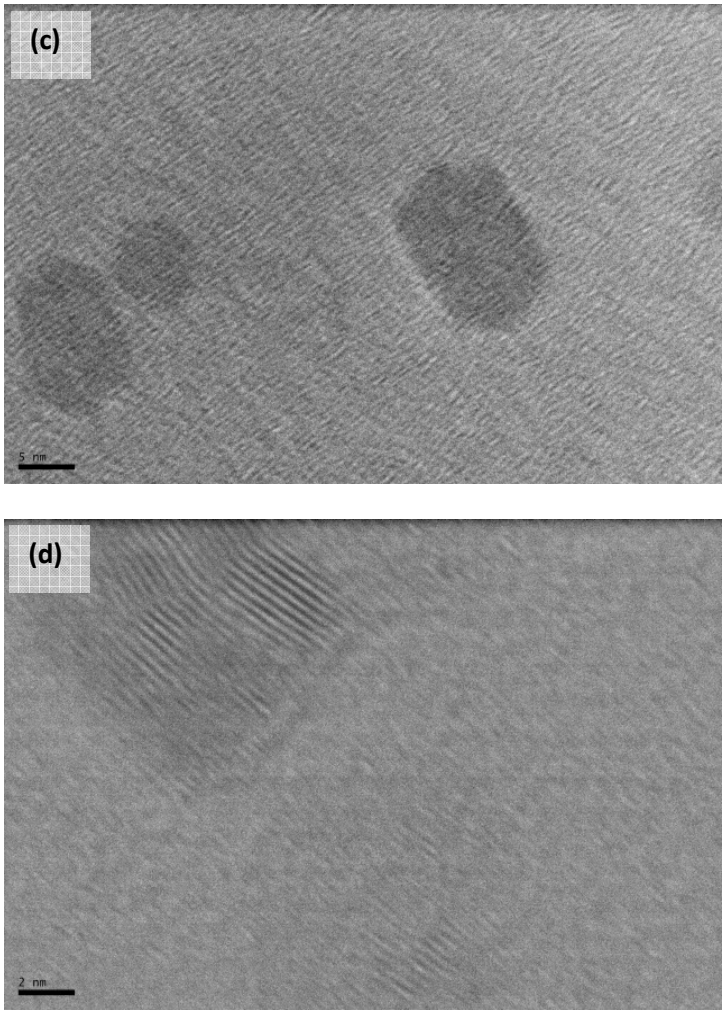

Figure 4.1: (a) Bright-field low-resolution TEM image (b), (c), (d) High-resolution images of anhydrously synthesized cerium-doped lanthanum fluoride colloidal NCs

The low-resolution image 4.1(a) confirms the presence of hexagonal platelets oriented both flat and side-on, exactly similar to the structure observed with the samples synthesized with chitosan. Image 4.1(b) shows that the nanocrystals have a significant size distribution, with various changing dimensions of the hexagonal sides. The mean size of the nanoparticles was found to be 13 nm, with a 4.5 nm (34%) standard deviation (from a statistical sample size of 50 nanocrystals from different images). Hence, a decrease in mean size and an appreciable increase in size distribution were observed

compared to the NCs synthesized with chitosan. This may be attributed to the absence of a thick coating layer, as was the case with the chitosan-capped samples. The high-resolution image 4.1(d) shows the atomic lattice planes on one of the flat-oriented nanocrystals. The fringe separation was measured to be 3.45 angstroms, which agreed with the value obtained for the chitosan-capped $LaF_3:Ce^{3+}$ NCs.

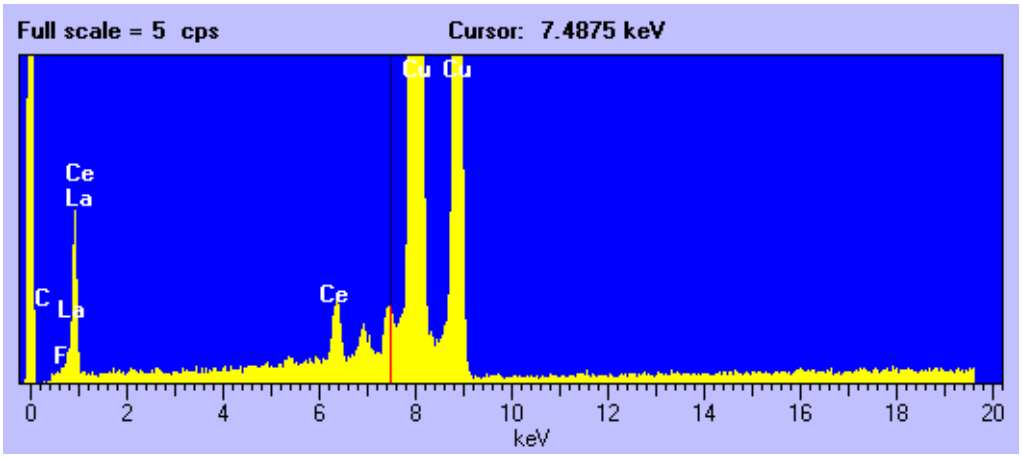

Figure 4.2: EDS spectrum of anhydrously synthesized cerium-doped lanthanum fluoride nanocrystals

The elemental presence of lanthanum, cerium, and fluorine was verified from the EDS spectrum, shown in Figure 4.2.

To verify the success of core/shell synthesis, the anhydrously synthesized core/shell nanocrystals were characterized using the transmission electron microscope. The images in ascending order of magnification are shown in Figure 4.3.

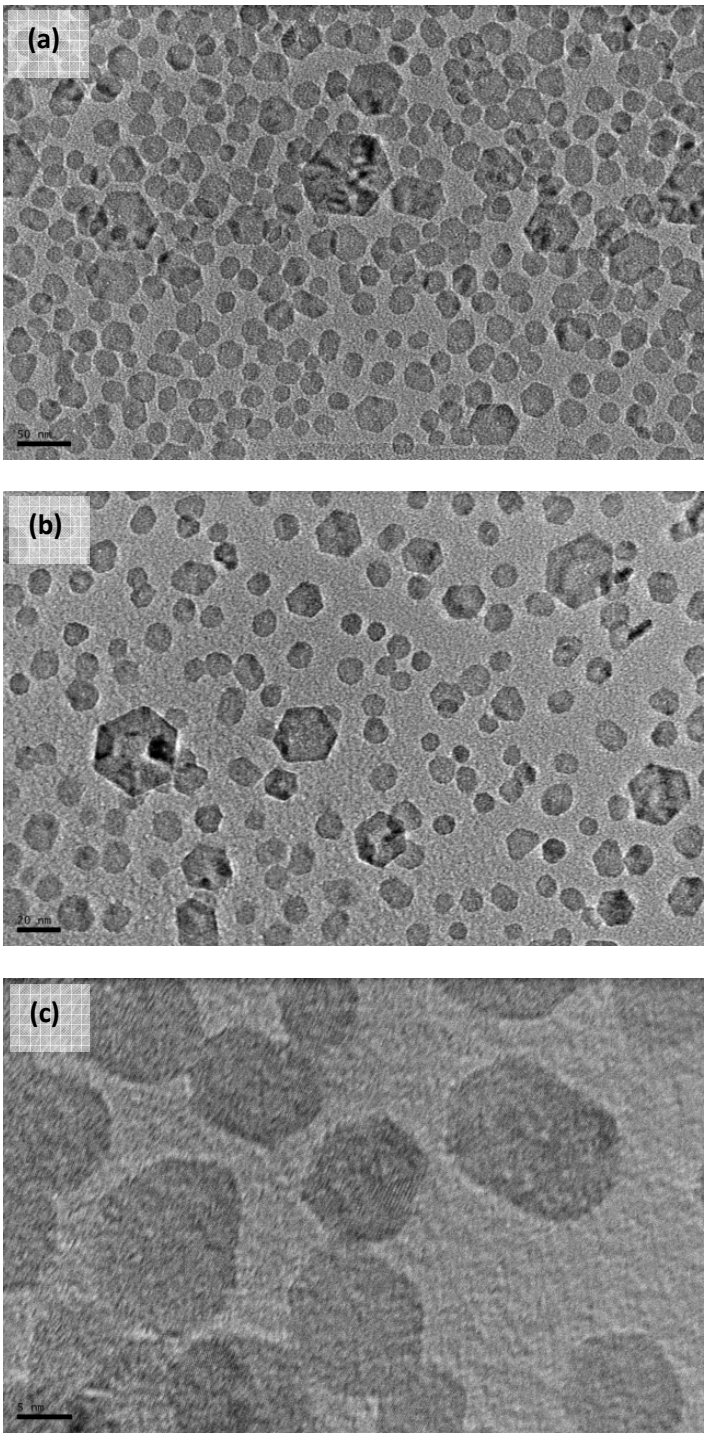
(a)
50 nm
(b)
20 nm
(c)
5 nm

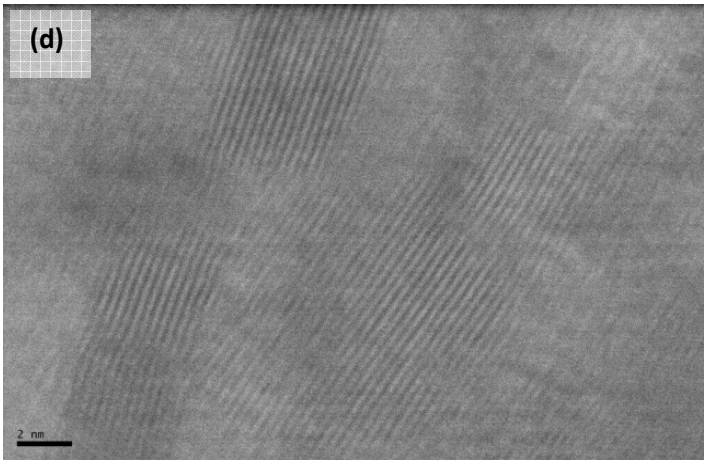

Figure 4.3: (a), (b) Bright-field low-resolution TEM images (c), (d) High-resolution images of anhydrously synthesized cerium-doped lanthanum fluoride/undoped lanthanum fluoride core/shell colloidal NCs with 50 nm, 10 nm, 5 nm, and 2 nm scale-bars respectively

The low-resolution images 4.3(a) and (b) show clear hexagonal platelets that are consistent with the structure of lanthanum fluoride core nanocrystals. The measured mean size of the core/shell NCs was 16 nm, with a standard deviation of 5.5 nm (34%) (from a statistical sample size of 50 nanocrystals from different images). Therefore, a 3 nm (23%) increase in size was observed in the core/shell NCs compared to the core-only NCs, while the size distribution remained constant at 34%. The measured fringe separation of 3.45 angstroms from the high-resolution image 4.3(d) also confirms the consistency of the values obtained from previous samples. There is no change in the fringe separation, the shell being the same material as the core.

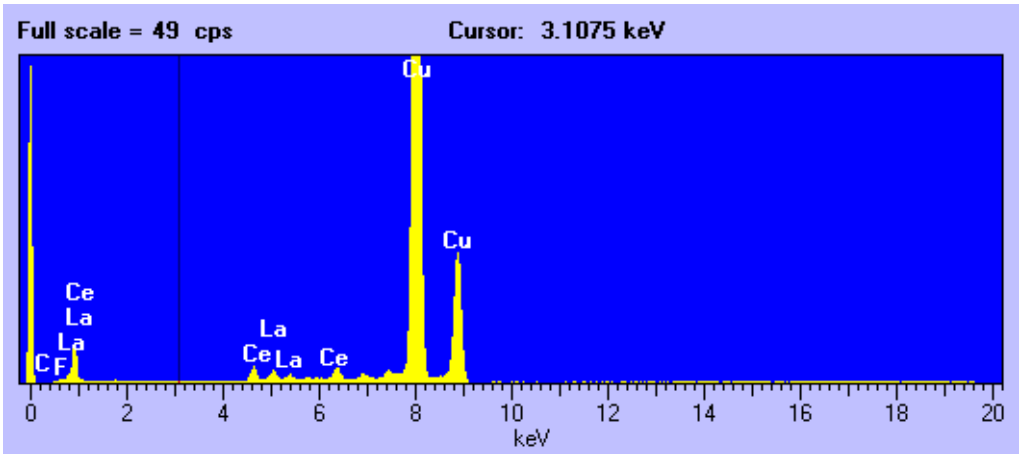

Figure 4.4: EDS spectrum of anhydrously synthesized cerium-doped lanthanum fluoride/undoped lanthanum fluoride core/shell nanocrystals

The elemental presence of lanthanum, cerium, and fluorine was verified from the EDS spectrum, shown in Figure 4.4. In conclusion, these results clearly indicate that the anhydrous core/shell synthesis in methanol was successful.

4.4. Optical characterization of anhydrously synthesized cerium-doped lanthanum fluoride core and core/shell colloidal nanocrystals

The optically translucent and viscous nature of the chitosan-capped nanocrystals was detrimental to the optical characteristic of the sample due to internal scattering and agglomeration over time. The main disadvantages of the samples synthesized through this method were their instability over time and internal scattering due to non-transparency of the sample. In contrast, the anhydrous synthesis produced optically transparent, non-viscous, and stable nanocrystal dispersion, as shown in Figure 4.5.

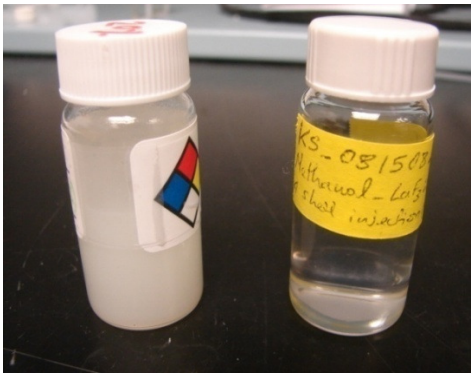

Figure 4.5: Anhydrous synthesis (right) produced a more stable and optically transparent colloidal dispersion compared to the aqueous synthesis (left)

Both core and core/shell nanocrystals were synthesized using the anhydrous route described in Section 4.1. The measured absorption spectra for the core and core shell samples are shown below in Figure 4.6.

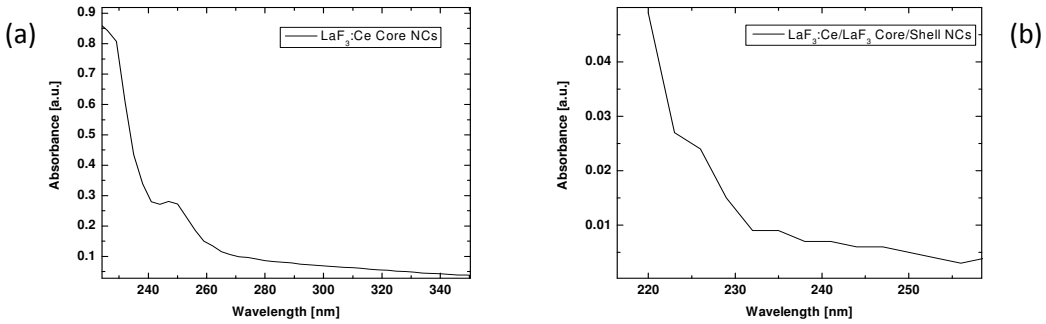

Figure 4.6: Absorption spectra of (a) core and (b) core/shell cerium-doped lanthanum fluoride NCs anhydrously synthesized in methanol

Absorption spectrum of the core sample shows absorption features around 250 nm while the spectrum of the core shell sample shows very weak features at about 225 nm, 235 nm, 242 nm, and 248 nm. The results confirm absorption in the internal energy levels of the cerium ions doped in the lanthanum fluoride core and core/shell nanocrystals.

However, the dilute nature of the samples was responsible for the weak absorption spectra.

The optimum excitation wavelength for both core and core/shell samples was 248 nm and 247 nm, respectively, as shown in the corrected PL excitation spectra, obtained with 1 nm excitation and emission slit widths (Figure 4.7).

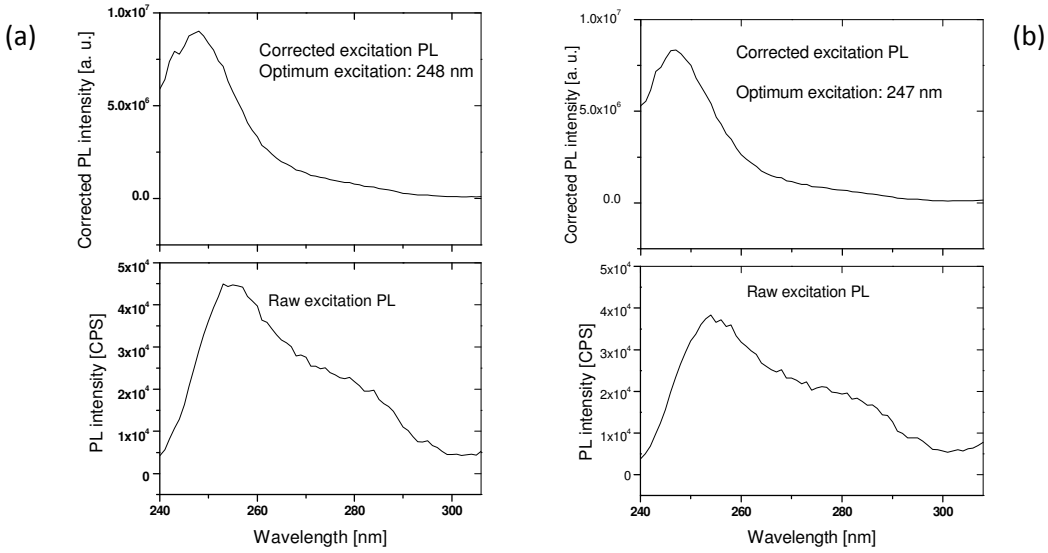

Figure 4.7: PL excitation spectra of (a) core and (b) core/shell cerium-doped lanthanum fluoride NCs anhydrously synthesized in methanol

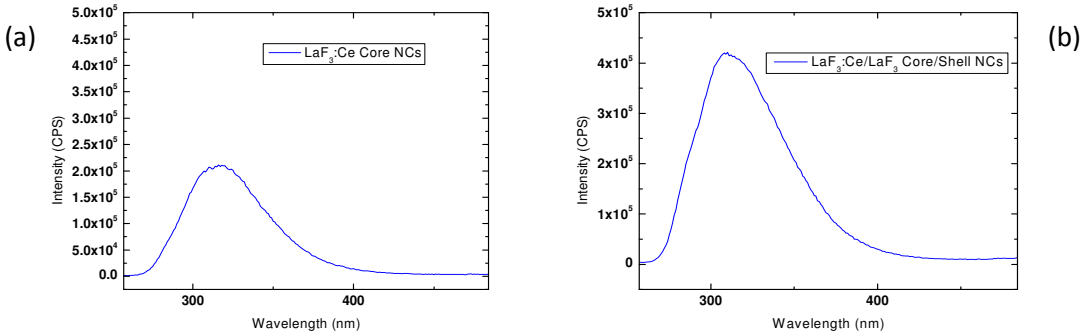

Figure 4.8: PL emission spectra of (a) core and (b) core/shell cerium-doped lanthanum fluoride NCs anhydrously synthesized in methanol

The PL emission spectra of the core and core/shell samples at 247 nm and 248 nm excitation wavelengths, respectively, with 1 nm excitation and emission slit widths, are given in Figure 4.8. The PL emission spectrum from the core NCs shows a peak at 319 nm with a full-width-to-half-maximum (FWHM) of 58 nm. The PL emission spectrum of core/shell NCs shows a similar spectrum with a slightly larger FWHM of 62 nm with about two-fold increase in intensity compared to the core. This clearly confirms the successful formation of the shell around the core since the higher PL intensity is expected to be due to the passivation of the surface defects that existed at the core-solvent interface, and the separation of the cerium activation centers from the high-vibrational solvent environment.

The PL lifetime is calculated by exponential curve fitting of the PL decay data, shown in Figure 4.9.

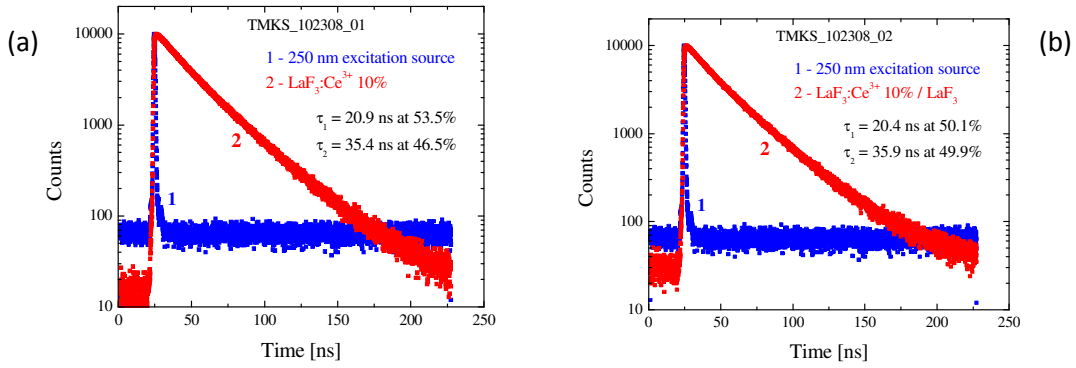

Figure 4.9: PL lifetime plots of (a) core and (b) core/shell cerium-doped lanthanum fluoride NCs anhydrously synthesized in methanol

As observed from the lifetime plots, there is no appreciable difference in lifetime between core and core/shell samples which is expected, since it is expected that there will be no change in the mechanism of emission in the cerium activation centers.

4.5. Summary

In summary, the structural characterization results verify that the anhydrous synthesis of 10% cerium-doped lanthanum fluoride core and core/shell NCs were both successful. The syntheses produced easily water-dispersible, stable, and optically transparent nanocrystals. Increase in size seen from TEM images and increase in PL emission intensity demonstrates the successful growth of undoped lanthanum fluoride shell through this anhydrous synthesis method, which is the underlying motive of this chapter.

References

1. DiMaio, J., B. Kokuoz, T.L. James, T. Harkey, D. Monofsky, and J. Ballato. “Photoluminescent characterization of atomic diffusion in core-shell nanoparticles” *Optics Express* 16, no. 16 (2008): 11769-11775.
2. van Veggel, F. C. J. M., and J. W. Stouwdam. "Improvement in the luminescence properties and processability of LaF_3/Ln and $LaPO_4$/Ln nanoparticles by surface modification" *Langmuir* 20, no. 26 (2004): 11763-11771.
3. Wang, Z., J. Bo, S. Song, L. Hu, J. Liu, and X. Zhen. "One-step synthesis of highly water-soluble LaF_3:Ln^{3+} nanocrystals in methanol without using any ligands" *Nanotechnology* 18, no. 46 (2007): 465606.

Chapter 5

Determination of optimum cerium content

5.1. Need for optimization

Bulk cerium fluoride has been discovered as a fast and high-density inorganic scintillator around 1990 (Anderson 1989), (Moses and Derenzo 1989), (Anderson 1990). When excited with 511 keV, the emission spectrum shows a double peak structure, with one peak near the material transmission cut-off at 300 nm (Moses and Derenzo 1990). The lifetime of this cerium emission peak was measured at about 2 to 10 ns, much shorter than the regular 27 ns component. For this reason, Moses *et al.* hypothesized that reducing the transmission cut-off by replacing some cerium ions with a similar material, (that has a higher bandgap) the faster short wavelength line of the cerium emission could be transmitted without being occluded. Further, the material should be crystallographically similar to cerium fluoride in order to maintain the crystal environment for the cerium ions. Lanthanum fluoride was an ideal material for this purpose since it has a low transmission cut-off at 125 nm (Mooney 1966) and it is also crystallographically very similar to cerium fluoride. This led to the idea of cerium-doped lanthanum fluoride as a source of the fast 300 nm emission (Moses and Derenzo 1990). Therefore, according to this hypothesis, a high proportion of cerium may lead to self-absorption of the short emission line.

Another consideration is the coupling of the electronic transitions between the molecular energy levels of the activation center with the vibrational modes of the host crystal. Since it is believed that the *5d* → *4f* electronic transition in cerium is protected from being quenched by the low vibrational energy of the lanthanum fluoride host lattice

(Dorenbos 2000A), (Dorenbos 2000B), (Dorenbos 2000C), a higher proportion of cerium to lanthanum in the crystal lattice may lead to increased quenching of the cerium emission in spite of more activations centers available for emission. Considering this trade-off, evidently, there is an optimum cerium concentration in the $La_xCe_{1-x}F_3$ material system, which needs to be determined experimentally.

This chapter presents the experiments performed to determine the optimum cerium content in lanthanum fluoride NCs (with the experimental considerations) and their respective observations.

5.2. Cerium-content optimization experiments using aqueous synthesis method

Chitosan-capped, cerium-doped lanthanum fluoride NCs were synthesized as given in Chapter 3. While maintaining all other synthesis parameters constant, seven different syntheses were performed with the cerium content (x) at 0.5%, 5%, 10%, 15%, 20%, 25%, 75%, and 100% with respect to the total lanthanide (cerium + lanthanum) content ($Ce_xLa_{1-x}F_3$). The PL emission spectra were measured for all the samples with 250 nm excitation using characterization methods described in Chapter 2.

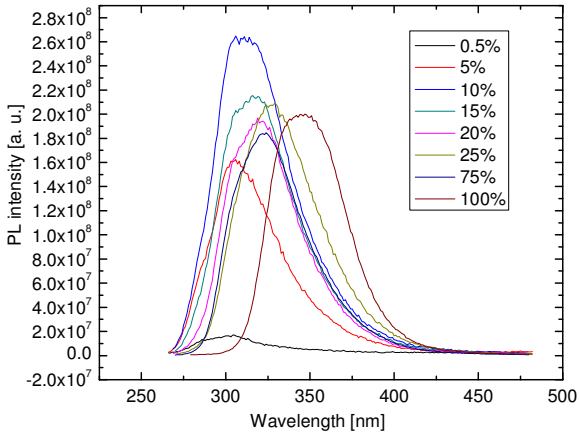

Figure 5.1: PL emission spectra of chitosan-capped lanthanum fluoride NCs at various cerium contents

PL spectra (Figure 5.1), obtained with 0.5 nm excitation and emission monochromator slit widths, show similar spectra in terms of shape and full-width-at-half-maximum for all cerium concentrations. When, the spectra were re-plotted as a function of photon energy rather than the wavelength, the observed spectral shape was close to a gaussian distribution, which is expected for 5d → 4f atomic-level transitions in cerium.

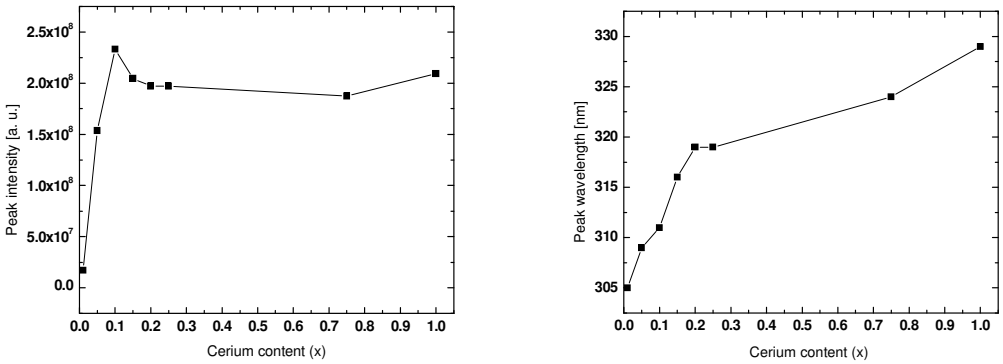

Figure 5.2: Variation of peak emission intensity and wavelength in chitosan-capped lanthanum fluoride $Ce_xLa_{1-x}Fe$ NCs with increasing cerium content (x)

The peak emission intensity and wavelength are plotted for increasing cerium content in Figure 5.2. An optimum is observed at 10% cerium concentration. A sharp fall off in intensity is observed for the 5% and 1% samples, whereas the emission intensity for higher concentration samples decreased only slightly. The peak emission wavelength red shifted with increasing cerium concentration while an almost constant peak was observed in the excitation spectra for all the samples.

In spite of maintaining all synthesis parameters, it was very difficult to maintain the concentration of the samples at the same level due to evaporation and sample loss during characterization. It was noticed that the intensity of emission significantly depended on the concentration of the sample and therefore it was imperative to normalize the concentration of all samples at high concentration by drying out the samples and re-dispersing the NCs to the exact same concentration in DI-water. The right-angle PL was measured and the sufficiency of concentration was determined by ensuring that almost no right-angle PL signal was observed.

5.3. Cerium-content optimization experiments using anhydrous synthesis method

In order to ensure reliability and repeatability of results, the optimization experiments were conducted on the samples synthesized using the anhydrous synthesis route. As mentioned in Chapter 4, these samples were more stable over time and optically clear in nature. This made it much easier to normalize concentration (concentration does not change if the NC dispersion is stable while doing measurements) and perform lossless

measurements. Both the excitation and emission monochromator slit widths were set to 0.5 nm. The results of PL measurements are given in Figure 5.3.

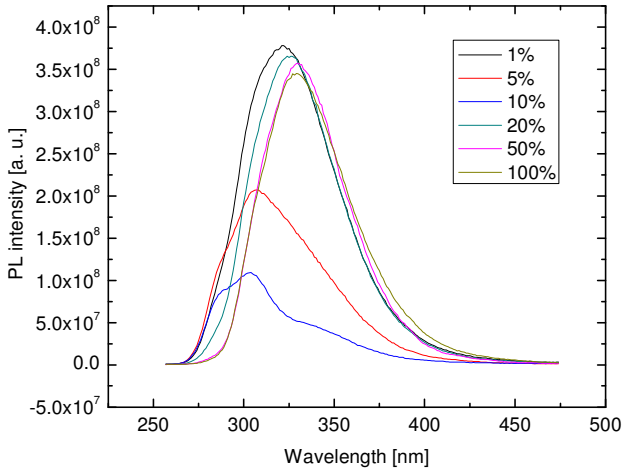

Figure 5.3: PL emission spectra of anhydrously synthesized lanthanum fluoride NCs at various cerium contents

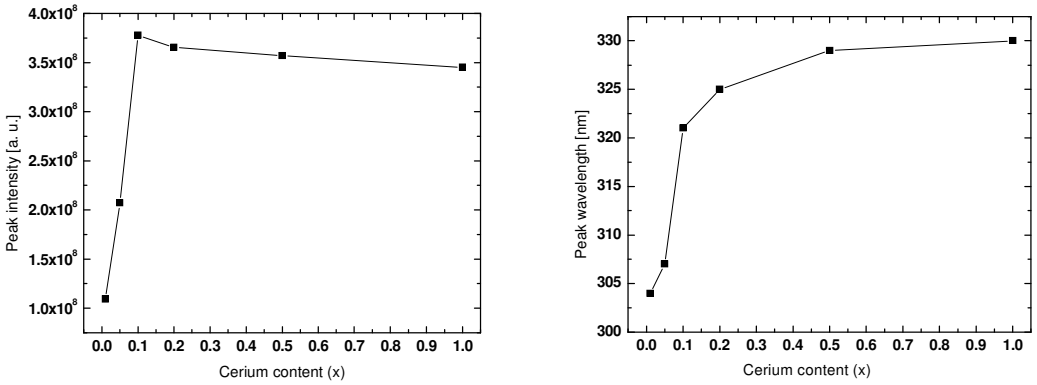

Figure 5.4: Variation of peak emission intensity and wavelength in anhydrously synthesized $Ce_xLa_{1-x}F_3$ NCs with increasing cerium content (x)

The results obtained from the anhydrously synthesized samples were very similar to those from the samples synthesized through the aqueous route. The peak excitation stayed

constant at 247 nm, again corresponding to the *4f* → *5d* excitation of cerium ions. The results also confirmed the optimum cerium concentration as 10% and the red shift of the peak emission wavelength with increasing cerium content was also repeatable (Figure 5.4). A possible explanation for the optimum cerium content and the red shift in PL emission is given in Section 5.4, inferred from the analysis of cerium concentration in bulk crystals.

5.4. Discussion

In 1994, Wojtowicz *et al.* provided a rigorous analysis of cerium emission in bulk lanthanum fluoride crystals. According to them, the emission from $Ce_xLa_{1-x}F_3$ crystals can be described through three processes: direct excitation of Ce^{3+} ions by UV excitation, ionization of Ce by high-energy radiation, formation of Ce bound excitons and subsequent transfer of carriers to Ce activator levels, and by the transfer of the lattice excitons of the host to the activator levels that leads to cerium ion emission (Wojtowicz *et al.* 1994). It is significant to note that in all the three processes, the final emission occurs from the Ce activator levels, although the excitation can be through different routes. In this case, it is evident from the excitation peak of 10% cerium-doped sample (given in Chapter 4) that the cerium ion inter-configurational *f* → *d* level is directly excited. While studying Nd^{3+}, Er^{3+}, and Tm^{3+} ions in trifluorides, Yang and DeLuca reported again the expectation that under ionizing excitation, the parity forbidden *f* → *f* transitions prevail over the parity allowed *d* → *f* transitions (Yang and DeLuca 1978), (Dorenbos *et al.* 1990). However, the excitation spectra of Ce^{3+} in lutetium fluoride confirmed that the lattice to activator transferred *d* → *f* emission is predominant owing to

the lower lying d level of cerium ion compared to other lanthanides (Heaps *et al.* 1976). Furthermore, while studying pure cerium fluoride, the fast (2-5 ns) emission was attributed to perturbed cerium ions (Ce_{per}) (Wojtowicz *et al.* 1992). Studies also suggested that the Ce_{per} channel competed with the activator emission by non-radiatively acquiring the carriers from the 5d levels (Pedrini *et al.* 1992).

This is consistent with the observed PL emission spectrum of the methanol based, 1% cerium-doped lanthanum fluoride NCs which is believed to be a superposition of three peaks corresponding to different emission routes. The shorter-wavelength ~285 nm peak is expected to be due to transitions terminating on the spin-orbit split $^2F_{5/2}$ and $^2F_{7/2}$ states of the *f* orbital as described in literature (Kroger and Bakker 1941), the ~ 303 nm emission is attributed to the 5d → 4f cerium ion activator levels, and the longer-wavelength ~340 nm broad line arises from the perturbed cerium ion levels. This also explains the red-shift in the spectra with increasing cerium content, since at higher concentrations more lattice-perturbed cerium ions are expected, which then can acquire carriers from the activator levels and therefore tend to shift the emission more towards the longer wavelength component as described above. This information is therefore useful in characterizing the synthesized cerium-doped NCs through the observation of already understood emission mechanism of cerium in bulk lanthanum halide crystals and to determine the optimum cerium concentration that produces the fast and efficient emission from cerium activator levels.

References

1. Anderson, D. F. "Properties of high-density scintillator cerium fluoride" *IEEE Trans. Nucl. Sci.* NS-36 (1989): 137-140.
2. Anderson, D. F. "Cerium fluoride, a scintillator for high-rate applications" *Nucl. Instr. Meth.* A-287 (1990): 606-610.
3. Dorenbos, P. "5*d* level energies of Ce^{3+} and the crystalline environment" *Phys. Rev. B* 62, no. 27 (2000A): 15640-15649.
4. Dorenbos, P. "The $4f^n \leftrightarrow 4f^{n-1}$ 5*d* transitions of the trivalent lanthanides in halogenides and chalcogenides" *J. Luminescence* 91, no. 12 (2000B): 91-106.
5. Dorenbos, P. "The 5d level positions of the trivalent lanthanides in inorganic compounds" *J. Luminescence* 91, no. 5 (2000C): 155-176.
6. Dorenbos, P., C. W. E. van Eijk, R. W. Hollander, and P. Schotanus. "Scintillation properties of Nd^{3+} doped LaF_3 crystals" *IEEE Trans. Nucl. Sci.* 37, no. 2 (1990): 119-124.
7. Heaps, S., L. R. Elias, and L. M. Yen. "Vacuum-ultraviolet absorption bands of trivalent lanthanides in LaF_3" *Phys. Rev. B.,* 13, no. 1 (1976): 94-99.
8. Kroger, F. A., and J. Bakker "Luminescence of cerium compounds" *Physica* 8, no. 7 (1941): 628-633.
9. Mooney, J. B. "Some properties of single crystal lanthanum trifluoride" *Infrared Physics* 6, no. 11 (1966): 153-157.
10. Moses, W. W., and S. E. Derenzo. "Cerium fluoride, a new fast, heavy scintillator" *IEEE Trans. Nucl. Sci.* NS-36 (1989): 173-176.

11. Moses, W. W., and S. E. Derenzo. "The scintillation properties of cerium-doped lanthanum fluoride" *Symposium on radiation measurements and applications.* Ann Arbor: DOE, (1990).

12. Pedrini, C., B. Moine, J. C. Gacon, and B. Jacquier. "One-and two-photon spectroscopy of Ce^{3+} ions in LaF_3-CeF_3 mixed crystals" *J. Phys.: Condensed Matter* 4, no. 4 (1992): 5461-5471.

13. Wojtowicz, A. J., E. Berman, Cz. Koepke, and A. Lempicki. "Stochiometric cerium compounds as scintillators" *IEEE Trans. Nucl. Sci.* 39, no. 4 (1992): 494-501.

14. Wojtowicz, A. J., M. Balcerzyk, E. Berman, and A. Lempicki. "Optical spectroscopy and scintillation mechanisms of $Ce_xLa_{1-x}F_3$" *Phys. Rev. B* 49, no. 21 (1994): 880-884.

15. Yang, K. H., and J. A. DeLuca. "Vacuum-ultraviolet excitation studies of $5d^1 4f^{n-1}$ to $4f^n$ and $4f^n$ transitions of Nd^{3+}, Er^{3+}, and Tm^{3+} doped trifluorides" *Phys. Rev. B* 17, no. 11 (1978): 4246-4255.

Chapter 6

Radiation hardness testing

6.1. Significance of radiation hardness

A necessary requirement for a material to be a good scintillator that can be used in radiation detection applications is its ability to absorb the high-energy radiation. Further while encountering this radiation, the fast moving ionizing particles of the radiation can damage the crystalline lattice of the absorbing material. Therefore, prolonged exposure to high-energy radiation is can easily degrade most crystalline material by knocking out atoms from the lattice thereby creating vacancies and defects. The property of a material to resist degradation in structural and optical properties when exposed to high-energy radiation is known as radiation hardness.

Since one of the major applications of cerium-doped lanthanum halide NCs is radiation detection, it is important to test the radiation hardness of the material and compare with a standard material. For the purpose of comparison, cadmium selenide NCs were used since they are proven to be one of the highly luminescent fluorescent NCs. CdSe/ZnS QDs have also been suggested as scintillators for detection of alpha particles and gamma rays (Létant and Wang 2006A), (Létant and Wang 2006B). In this chapter, the effects of gamma-irradiation on photoluminescent properties of cerium-doped lanthanum fluoride NCs and CdSe/ZnS QDs are reported and compared.

6.2. Sample preparation

Chitosan-capped lanthanum fluoride NCs doped with 5% cerium were synthesized as described in Chapter 3. CdSe cores were synthesized according to a modified procedure given by (Aldana *et al.* 2001). First, the cadmium precursor (cadmium acetate) was dissolved in a coordinating solvent, trioctylphosphine oxide (TOPO). The solution was heated in a flask under controlled argon atmosphere to 325 °C, while a solution of selenium in trioctylphosphine (TOP) and toluene was prepared in an argon-filled glovebox with < 0.1 ppm of water vapor and oxygen. When the temperature of the solution in the flask reached 325 °C, the selenium precursor solution was rapidly injected into the flask. When the contents of the flask reached red color, the solution was cooled to room temperature by removing the heat source. CdSe cores were precipitated in a centrifuge using acetone and methanol, and collected in hexanes. For ZnS coating, the zinc precursor was prepared by dissolving the zinc alkyl alkoxide (ZnONEP) with oleic acid and octadecene, while the sulfur precursor was prepared by dissolving sulfur in octadecene. Both precursors were heated to 200-250 °C and the zinc precursor was cooled to 60-80 °C, while the sulfur precursor was cooled to room temperature. The CdSe nanocrystals in hexanes were mixed with octadecene and octadecylamine in a flask and heated to 100 °C under vacuum for 30 minutes and then under argon to 240 °C. At that point, three alternating injections of calculated amounts of zinc and sulfur precursors were made at 10-minute intervals. Finally the solution was cooled to room-temperature; QDs were precipitated with acetone and methanol, and collected in hexanes.

6.3. Experimental setup for gamma-radiation exposure

An Eberline 1000B multiple-source gamma calibrator was used. In order to accelerate the degradation process, the strongest of the available sources was used, namely a ^{137}Cs source with the activity of 39.7 Ci (calibrated with Canberra RADIACMETER®), emitting 662 keV γ rays. Using the most powerful source available on the calibrator, a flux rate of 97.3 roentgens/hr was measured at the original test position of seven inches above the floor of the exposure chamber. At certain point, samples were moved to the floor of the exposure chamber shown in Figure 6.1, which raised the gamma flux to 330.8 roentgens/hr.

Figure 6.1: NC samples placed inside the Eberline 1000B multiple source γ calibrator (A ^{137}Cs 662 keV γ ray source was used for the experiment)

Using a Horiba Jobin Yvon Fluorolog-3 spectrofluorometer, PL measurements were performed after certain periods of irradiation to check if the nanocrystals exhibited any signs of degradation in their optical characteristics. In order to exclude the effect of natural degradation due to oxidative processes on PL properties of the nanocrystals, two identical samples were prepared for each material under test, cerium-doped lanthanum fluoride and cadmium selenide/zinc sulfide NCs. Their PL spectra were measured prior to

irradiation experiments, thus establishing the base line for monitoring PL dynamics under irradiation. One of the samples was then irradiated, while the other one, called the "control" sample, was stored under RT conditions to be used for comparison purposes. Assuming that both irradiated and control samples undergo the same aging process and react to environmental changes in the same way, the results of PL degradation measurement of the irradiated sample were corrected for any changes in PL intensity of the control sample with respect to its base line measurement.

The total exposure of the nanocrystals needs to be converted to absorbed dose for comparison to other scintillation materials. Converting roentgens for a monoenergetic source into rads for a particular material *x* can be done using energy absorption coefficients (Cattaneo 1991) as follows:

$$D = 0.88 \times E \times \frac{\left(\frac{\mu_{en}(h\nu)}{\rho}\right)_x}{\left(\frac{\mu_{en}(h\nu)}{\rho}\right)_{air}} \tag{6.1}$$

where D is the dose in rads, E is the exposure in roentgens, $h\nu$ is the γ photon energy, ρ is the density of the material x, and $\mu_{en}(h\nu)/\rho$ is the energy absorption coefficient for the subscripted material.

6.4. Results and discussion

The effect of gamma irradiation on the lanthanum fluoride and cadmium selenide/zinc sulfide samples in terms on PL emission intensity is given in Figure 6.2.

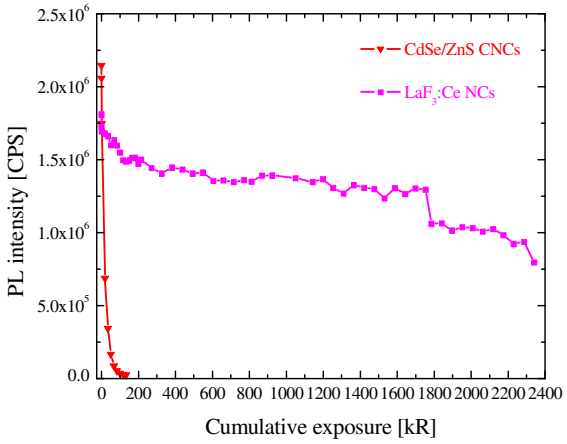

Figure 6.2: Variation of PL emission intensity with exposure dose to gamma-radiation for lanthanum fluoride NCs doped with 5% cerium and cadmium selenide/zinc sulfide NCs

As observed in Figure 6.2, CdSe/ZnS QDs, initially very bright, showed a rapid loss of light output when exposed to 662 keV γ rays, and were removed from the experiment after 133.2 kR cumulative exposure. In terms of the absorbed dose, the CdSe/ZnS NCs turned out to be of very poor radiation hardness, having lost 50% of their light output after only ~11.5 krad of absorbed dose [equivalent to ~11.3 krad(Si)], rendering them unsuitable for aerospace and terrestrial applications where radiation hardness up to total γ-ray doses of 250 Mrad is a prerequisite. This should be contrasted with excellent radiation hardness of GaN/InGaN multiple-quantum-well LEDs, that can sustain 250 Mrad(Si) from ^{60}Co source with ~45% loss in their PL intensity (Khanna *et al.*).

In contrast to CdSe/ZnS NCs, cerium-doped lanthanum fluoride NCs exhibited excellent radiation hardness after an extended exposure dose of about 2400 krads, as shown in Figure 6.2. PL intensity loss was about 45% of the original intensity of non-

irradiated sample after 2400 krads of absorbed dose for cerium-doped lanthanum fluoride NCs. In direct comparison, the CdSe/ZnS NCs lost almost 50% of their light output just after ~11.5 krad of absorbed dose whereas the lanthanum fluoride NCs doped with 5% cerium lost only ~20.5% of their light output even after 722 krad of absorbed dose.

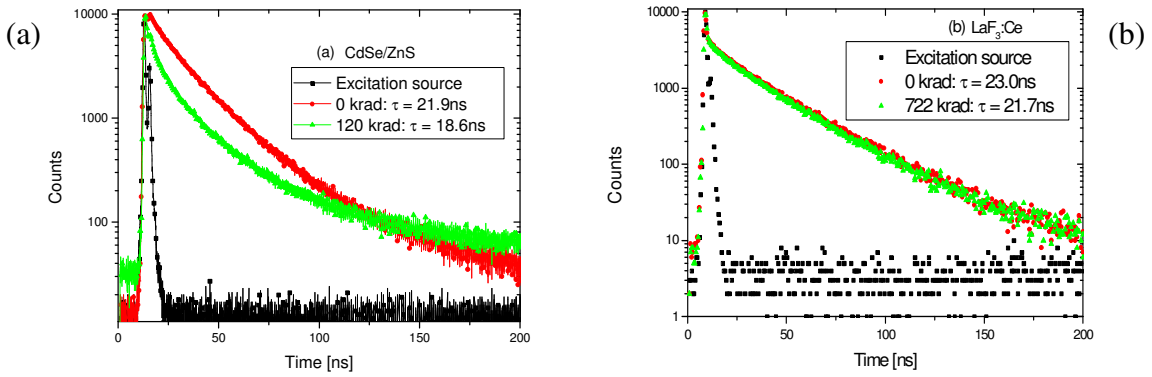

Figure 6.3: Effects of γ irradiation on PL lifetime for (a) CdSe/ZnS NCs and (b) chitosan-capped lanthanum fluoride NCs doped with 5% cerium

An average PL lifetime of 21.9 ns was measured for the control sample of CdSe/ZnS NCs, reducing to 18.6 ns after 120 krad irradiation (Figure 6.3), with accompanying dramatic reduction of quantum yield from 23.4% to 0.2%. The same tendency of the PL lifetime becoming shorter after irradiation was observed in cerium-doped lanthanum fluoride NCs, although to a much lesser extent and after a much larger dose, which is consistent with the less significant radiation damage incurred in these nanocrystals, as inferred from the PL light output results. A PL lifetime of 23 ns was observed for the control sample of $LaF_3:Ce^{3+}$ NCs and a shorter lifetime of 21.7 ns was measured for the irradiated sample after 722 krad of dose. These observations can be explained as the influence of nonradiative recombination centers created in the irradiated materials.

Therefore, the cerium-doped lanthanum fluoride NCs are proved to possess excellent radiation hardness to gamma irradiation and can be reliably used as gamma radiation detectors.

References

1. Aldana, J., Y. A. Wang, and X. G. Peng. "Photochemical instability of CdSe nanocrystals coated by hydrophilic thiols" *J. Am. Chem. Soc.* 123, no. 36 (2001): 8844-8850.
2. Cattaneo, P. W. "Calibration procedure for irradiation tests on silicon devices" *IEEE Trans. Nucl. Sci.* 38, no. 3 (1991): 894-900.
3. Khanna, R., S. Y. Han, S. J. Pearton, D. Schoenfeld, W. V. Schoenfeld, and F. Ren. “High dose Co-60 gamma irradiation of InGaN quantum well light-emitting-diodes” Appl. Phys. Lett. 87, no. 2 (2005): 2107-2122.
4. Létant, S. E., and T. -F. Wang. "Semiconductor quantum dot scintillation under gamma-ray irradiation" *Nano Letters* 12, no. 4 (2006A): 1-12.
5. Létant, S. E., and T. -F. Wang. "Study of porous glass doped with quantum dots or laser dyes under alpha irradiation" *Appl. Phys. Lett.* 88, no. 1 (2006B): 103-110.

Chapter 7

Synthesis and characterization of anhydrously synthesized cerium-doped lanthanum bromide core and core/shell colloidal nanocrystals

7.1. Anhydrous synthesis of cerium-doped lanthanum bromide colloidal nanocrystals

Bulk cerium-doped lanthanum bromide crystals possess unique excellent scintillation properties that excite the gamma ray detection community. The possibility to discern between gamma rays of slightly different energies is of great importance to a sensitive scintillation detector. This characteristic of a scintillating material is known as energy resolution. It is reported in literature that among all the available scintillating materials, cerium-doped lanthanum bromide has the highest energy resolution with the least full width to half maximum (3.2%) when excited with 662 keV gamma rays (Shah *et al.* 2003). In conjunction with this unique advantage, cerium-doped lanthanum bromide crystals have also been reported to possess a very high light yield (about 63,000 photons/MeV) and a fast decay time of less than 30 ns (Liu *et al.* 2007). Therefore, it is of particular interest to demonstrate the successful synthesis of nanoscale colloidal nanocrystals of cerium-doped lanthanum bromide. Since lanthanum bromide is highly hygroscopic and it needs to be synthesized anhydrously, methanol was used as the synthesis medium, as described in this chapter. A successful synthesis of cerium-doped

lanthanum bromide nanocrystals through an anhydrous synthesis route was carried out, as detailed in the following sections.

7.1.1. Synthesis

Cerium-doped lanthanum bromide nanocrystals were synthesized using a procedure directly adapted from the synthesis technique for hydrophilic cerium-doped lanthanum fluoride nanocrystals (Wang *et al.* 2007) by replacing fluorine with bromine. A major difference between lanthanum fluoride and lanthanum bromide is the highly hygroscopic property of the latter. Therefore, the material could not be synthesized using any of the usual hydrothermal processes performed in an aqueous solution. However, this synthesis was possible since the anhydrous method (Section 4.1) was designed to be performed entirely under a controlled water-free atmosphere using the Schlenk line and glovebox.

7.1.2. Basic chemical reaction

The following is the basic chemical reaction that is expected to occur during the nucleation phase of the anhydrous synthesis of cerium-doped lanthanum bromide NCs.

$$CH_3OH + 1\ \text{mmol}\ (La(NO_3)_3 + Ce(NO_3)_3) + 3\ \text{mmol}\ NH_4Br \rightarrow 3\ \text{mmol}\ NH_4NO_3 + 1\ \text{mmol}\ \mathbf{LaBr_3{:}Ce^{3+}/OH}$$

7.1.3. Preparation of precursors

All precursors were prepared inside the glovebox. Lanthanum nitrate hexahydrate 99.99%, cerium nitrate heptahydrate 99.999%, ammonium bromide 99.9%, and anhydrous absolute methanol 99.9% were purchased from Sigma Aldrich Co. and used as such. A 0.65 M lanthanide precursor solution was prepared by dissolving 1.3 mmol total of lanthanum nitrate hexahydrate and cerium nitrate heptahydrate in 2 mL of anhydrous

methanol. The bromine precursor solution was prepared by dissolving 3 mmol of ammonium bromide in 35 mL of anhydrous methanol in a three-neck round-bottom borosilicate flask.

7.1.4. Synthesis procedure

A synthesis procedure similar to cerium-doped lanthanum fluoride core and core/shell NCs was used to synthesize cerium-doped lanthanum bromide core and core/shell NCs with the exception of replacing the fluorine precursor, ammonium fluoride in the earlier case with the bromine precursor, ammonium bromide in this case. The three-neck flask containing the bromide precursor in anhydrous methanol was taken out from the glovebox, connected to the Schlenk line, and heated to 60 °C at the rate of 5 °C/min. After the temperature reached 60 °C, the lanthanide (lanthanum + cerium) precursor was injected rapidly into the flask. The solution was allowed to stir at 1000 rpm for 2 hours under argon atmosphere after which the flask was cooled down, taken into the glovebox, and the solution was transferred to several 20 mL scintillation vials. All samples for characterization were prepared inside the glovebox, avoiding any exposure to water.

7.2. Anhydrous synthesis of cerium-doped lanthanum bromide/undoped lanthanum fluoride core/shell colloidal NCs

The shell procedure from Section 4.2 was further extended to the core/shell synthesis of cerium-doped lanthanum bromide/undoped lanthanum fluoride colloidal NCs. Lanthanum fluoride was selected as the shell material due to its stable nature and since its bandgap is almost two times larger than lanthanum bromide (Gao and Michael 2008).

The hydroxyl groups being efficient non-radiative recombination centers, they tend to effectively quench the light emission originating from cerium ions (van Veggel and Stouwdam 2004). Therefore, it is essential to have a thick shell coating to improve the photoluminescence intensity. Apart from the main role of shielding the highly hygroscopic lanthanum bromide core from moisture (and therefore making them usable in air), the undoped LaF_3 shell also provides good quantum confinement.

7.2.1. Synthesis

Cerium-doped lanthanum bromide/undoped lanthanum fluoride core/shell nanocrystals were synthesized using the anhydrous core/shell synthesis procedure in methanol given in section 4.2 by replacing fluoride core precursor (ammonium fluoride) with bromide core precursor (ammonium bromide), while maintaining the same molar quantities. The entire synthesis was again performed under a controlled water-free atmosphere using the Schlenk line and glovebox. Both core and shell precursors were prepared inside the glovebox and taken out using syringes. In order to compare the core and core/shell, the core-only aliquot of cerium-doped lanthanum bromide NCs in anhydrous methanol was taken before injecting the shell precursors.

7.2.2. Basic chemical reactions

The following gives the balanced chemical reactions that are expected to occur during the anhydrous synthesis of cerium-doped lanthanum bromide/undoped lanthanum fluoride core shell NCs.

CH_3OH + 1 mmol ($La(NO_3)_3$ + $Ce(NO_3)_3$) + 3 mmol NH_4Br → 3 mmol NH_4NO_3 + 1 mmol **$LaBr_3:Ce^{3+}$/OH**

$LaBr_3:Ce^{3+}$/OH+4 mmol $La(NO_3)_3$+12 mmol NH_4F → 12 mmol NH_4NO_3 + 1 mmol **$LaBr_3:Ce^{3+}/LaF_3$/OH**

7.2.3. Preparation of precursors

All precursors were prepared inside the glovebox. Lanthanum nitrate hexahydrate 99.99%, cerium nitrate heptahydrate 99.999%, ammonium bromide 99.9%, ammonium fluoride 99.9%, and anhydrous absolute methanol 99.9% were purchased from Sigma Aldrich Co. and used as such. A 0.65 M lanthanide precursor solution was prepared by dissolving 1.3 mmol total of lanthanum nitrate hexahydrate and cerium nitrate heptahydrate in 2 mL of anhydrous methanol. The bromine precursor solution was prepared by dissolving 3 mmol of ammonium bromide in 35 mL anhydrous methanol in a three-neck round-bottom borosilicate flask. The lanthanum precursor for the shell was prepared by dissolving 5.2 mmol of lanthanum nitrate hexahydrate in 8 mL of anhydrous methanol and the fluorine precursor for the shell was prepared similarly by dissolving 12 mmol of ammonium fluoride in 8 mL of anhydrous methanol.

7.2.4. Synthesis procedure

The three-neck flask containing the bromide precursor in anhydrous methanol was taken out from the glovebox, connected to the Schlenk line, and heated to 60 °C at the rate of 5 °C/min. After the temperature reached 60 °C, the lanthanide (lanthanum + cerium) precursor was injected rapidly into the flask. The solution was allowed to stir at 600 rpm for 10 minutes under argon atmosphere, after which 5 mL of core aliquot was taken out from the flask using an aliquot syringe. Then, alternate drop wise injections of lanthanum and fluorine shell precursors were done at the rate of 5 drops/min. The

solution in the flask was subsequently allowed to stir at 1000 rpm for 2 hours under argon atmosphere. After 2 hours, the solution was purified and precipitated by centrifugation at 5000 rpm using methanol, and dispersed in DI water. It was observed that the cerium-doped lanthanum bromide/undoped lanthanum fluoride core/shell NCs were highly dispersible in water due to the hydrophilic hydroxyl groups attached to lanthanum fluoride shell, and were also very stable without any signs of aggregation or flocculation. In contrast with the ability to store the core/shell sample in DI water after centrifugation, the core aliquot sample was stored as synthesized in methanol at room temperature in an air tight vial inside the glovebox. All samples for characterization of the core aliquot were prepared inside the glovebox, avoiding any exposure to water vapor.

7.3. Structural characterization of anhydrously synthesized cerium-doped lanthanum bromide and cerium-doped lanthanum bromide/undoped lanthanum fluoride core/shell NCs

Structural and elemental characterization was performed on the cerium-doped lanthanum bromide core and core/shell samples using TEM and EDS. Due to the highly hygroscopic nature of the lanthanum bromide NCs, special care was taken in preparation and handling of the TEM samples. The TEM samples were prepared inside the glovebox and the sample boxes were transported to the TEM facility using tightly sealed grid holders. The only exposure to atmosphere happened briefly while the sample was loaded into the microscope.

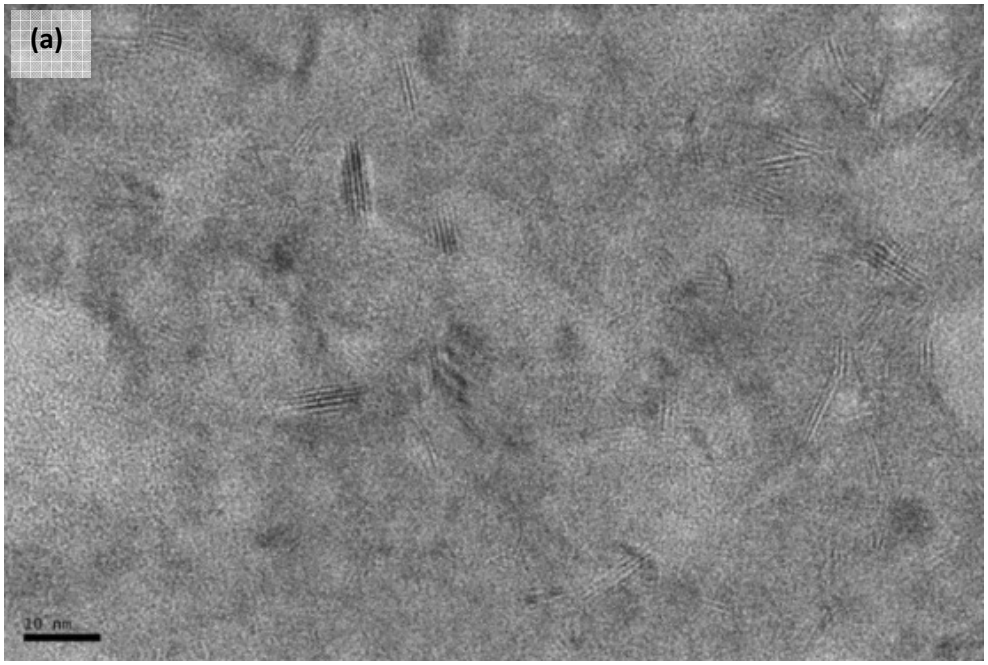
(a)
10 nm

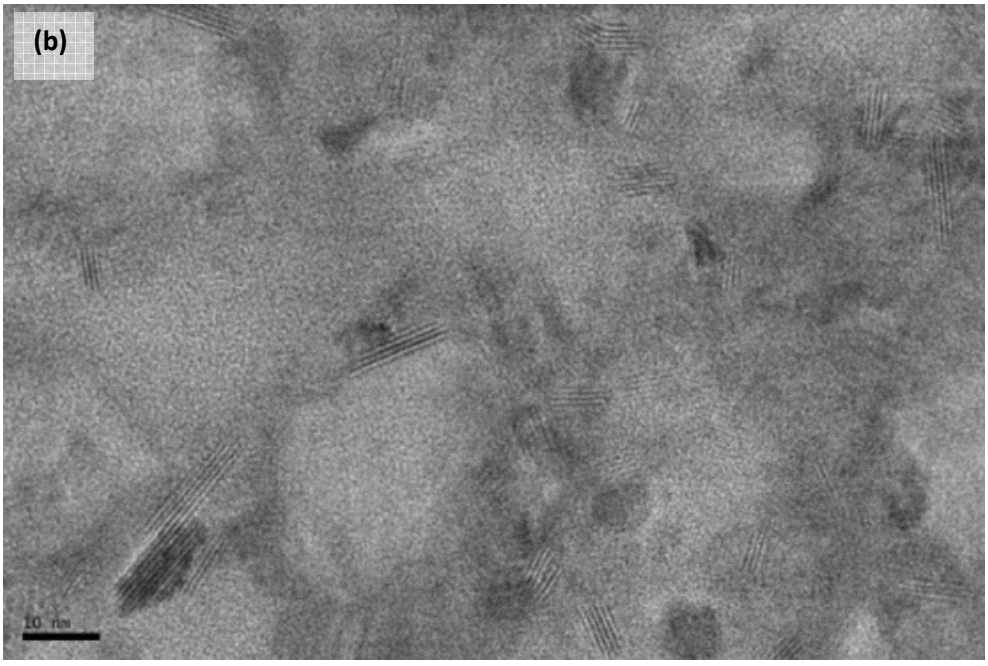
(b)
10 nm

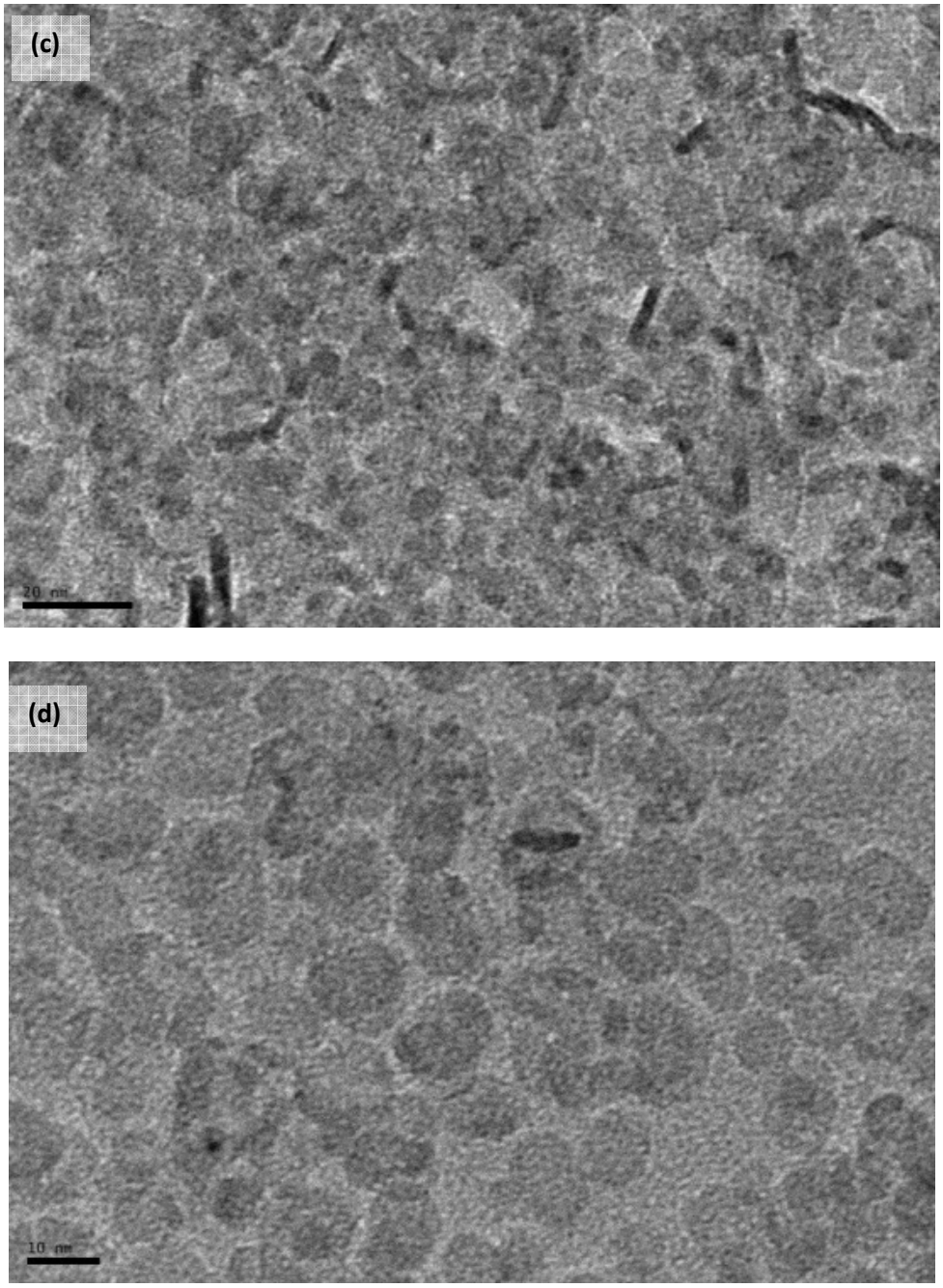

Figure 7.1: (a) and (b) High-resolution TEM images of anhydrously synthesized lanthanum bromide doped with 10% cerium NCs with 20 and 10 nm scale bars, respectively, (c) and (d) TEM images of anhydrously synthesized lanthanum bromide doped with 10% cerium core /undoped lanthanum fluoride shell NCs with 20 and 10 nm scale bars, respectively

The high-resolution TEM images in Figure 7.1(a) and (b) of the core sample confirm the presence of polydisperse single-crystal lanthanum bromide nanocrystals. The images of core NCs show an average size of 10.5 nm with a standard deviation of 2.8 nm (28%), while the images of core/shell NCs show a mean size of 14 nm with a standard deviation of 4 nm (28.5%) (from a statistical sample size of 50 NCs from different images for both core and core/shell samples). The core/shell NCs show hexagonal structures similar to the previously observed cerium-doped lanthanum fluoride structures, while the core images were limited to showing the high-resolution images of the side-on oriented NCs. However, the high-resolution images of the cerium-doped lanthanum bromide NCs enable the determination of the fringe-separation, which was measured to be 7.4 angstroms (from a statistical sample of 5 NCs from two different high-resolution images). The increased fringe-separation observed in cerium-doped lanthanum bromide NCs compared to that observed in cerium-doped lanthanum fluoride NCs is expected since the former has a lower bandgap compared to the latter, as summarized in Table 7.1.

Table 7.1: Bandgap and measured fringe-separation of lanthanum bromide and lanthanum fluoride

Material	**Bandgap** (Gao and Michael 2008)	**Fringe-separation measured from HR-TEM images**
Lanthanum fluoride	10.10 eV	3.45 angstroms
Lanthanum bromide	5.15 eV	7.4 angstroms

Therefore, it can be inferred from the table that there is a compressive strain on the active region (core) in the cerium-doped lanthanum bromide/lanthanum fluoride core/shell material system.

(a)

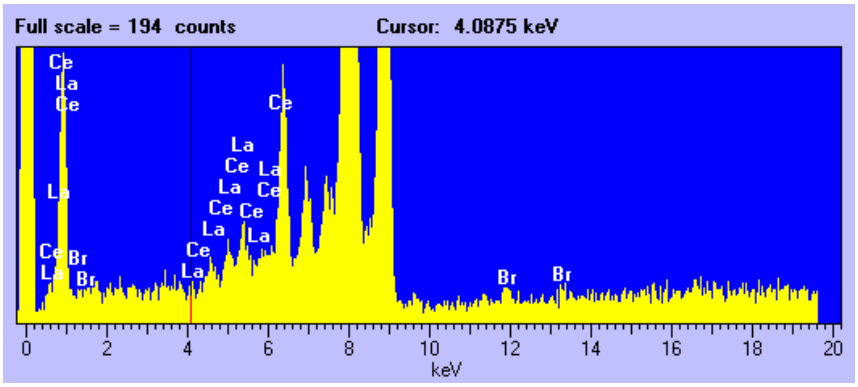

(b)

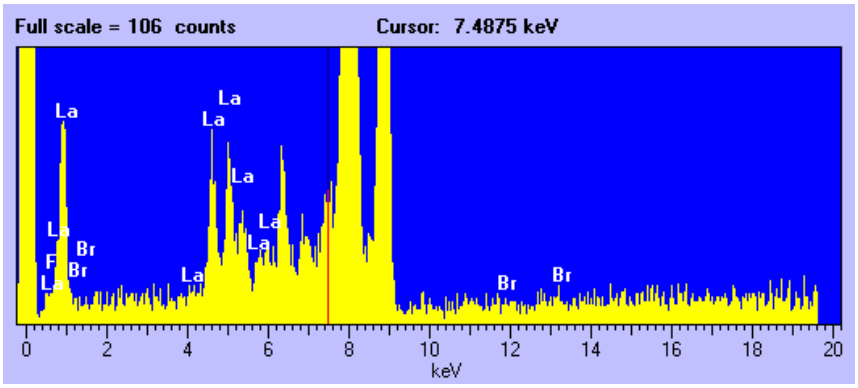

Figure 7.2: EDS spectrum of (a) lanthanum bromide doped with 10% cerium core NCs and (b) lanthanum bromide doped with 10% cerium core /undoped lanthanum fluoride shell NCs

The EDS spectrum shown in Figure 7.2 confirms the elemental presence of cerium, lanthanum, and bromine in the core sample and fluorine in addition to the above elements in the core/shell sample.

7.4. Optical characterization of anhydrously synthesized cerium-doped lanthanum bromide and cerium-doped lanthanum bromide/undoped lanthanum fluoride core/shell colloidal NCs

The results of absorption measurements for the core lanthanum bromide nanocrystals doped with cerium and core/shell with undoped lanthanum fluoride shell are shown in Figure 7.3.

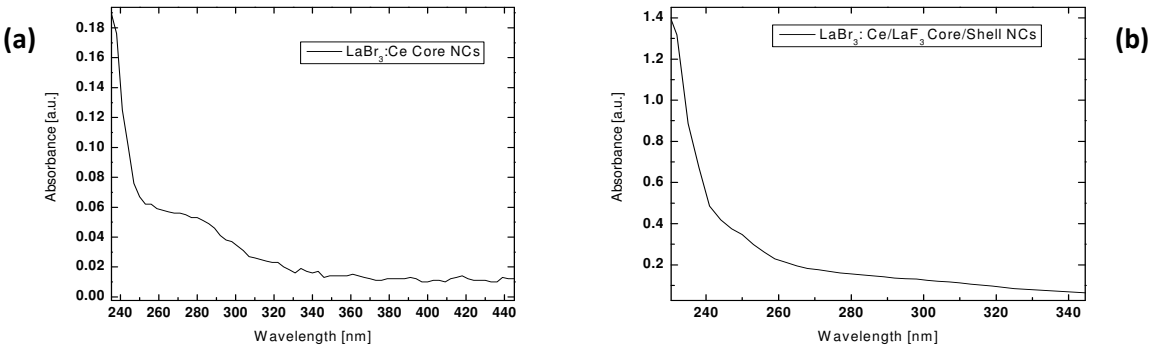

Figure 7.3: Absorption spectra of (a) anhydrously synthesized cerium-doped lanthanum bromide colloidal NCs and (b) anhydrously synthesized cerium-doped lanthanum bromide/undoped lanthanum fluoride core shell colloidal NCs

The measured absorption in Figure 7.3(a) was again very weak due to the dilute nature of the core sample. However, the figure shows an absorption feature at 280 nm and the absorption spectrum in Figure 7.3(b) shows a faint shoulder at 250 nm for the core/shell NCs. This confirms a change in effective absorption edge from the core NCs to core/shell NCs possibly due to lattice strain.

The PL excitation spectra of the core and core/shell samples are shown in Figures 7.4 (a) and (b) respectively, observed at 314 nm and 300 nm emission wavelengths,

respectively. The optimum excitation for the core NCs was 280 nm and that for the core/shell NCs was 247 nm. The PL emission spectra for core and core/shell NCs are given in Figures 7.5(a) and (b), respectively.

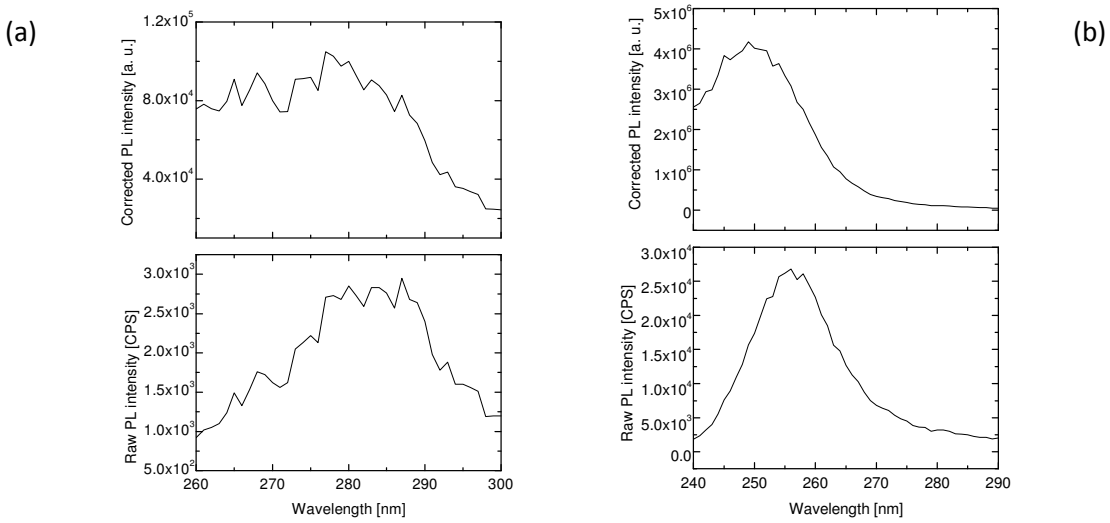

Figure 7.4: PL excitation spectra of (a) anhydrously synthesized cerium-doped lanthanum bromide NCs and (b) anhydrously synthesized cerium-doped lanthanum bromide/undoped lanthanum fluoride core/shell NCs

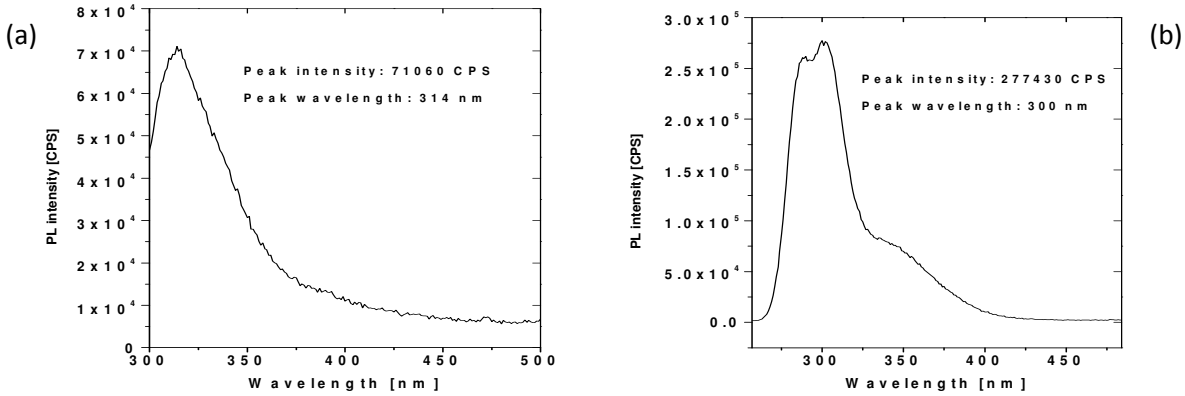

Figure 7.5: PL emission spectra of (a) anhydrously synthesized cerium-doped lanthanum bromide NCs and (b) anhydrously synthesized cerium-doped lanthanum bromide/undoped lanthanum fluoride core/shell NCs

The PL peak intensity of the core/shell NCs increased about 4 times and blue-shifted 14 nm compared to that of core NCs. The lower PL emission intensity of the core NCs can be explained due to the fact that the NCs were dispersed in methanol, which has, as already stated, efficient luminescence quenching property by providing non-radiative recombination centers. Furthermore, the blue-shift can be attributed to the compressive strain on the active core region due to the smaller effective lattice parameters of the shell material (reported lattice parameters of lanthanum fluoride: a = b = 7.185 angstroms, c = 7.351 angstroms) (Kruk *et al.* 2006) compared to that of the core material (reported lattice parameters of lanthanum bromide: a = b = 7.951 angstroms, c = 4.501 angstroms) (Liu *et al.* 2007). Another possible explanation of the significant change in spectra between the core and core/shell NCs is that the shell injections could lead to the formation of new lanthanum fluoride NCs, incorporating the unreacted cerium ions from the core synthesis reaction and effectively forming low cerium-doped lanthanum fluoride NCs. However, the validity of the latter explanation suffers from the fact that the PL emission spectrum of the core NCs is fairly narrow, as opposed to being broad which would be expected if there were remaining unreacted cerium ions in the solution (refer to free Ce ion emission shown in Figure 3.6). Therefore the former explanation bears more validity; however, beyond such experimental evidence, the theoretical proof of the same is beyond the scope of this work.

The lifetimes for the core and core/shell NCs are calculated similarly from the decay time scatter plots shown in Figure 7.6.

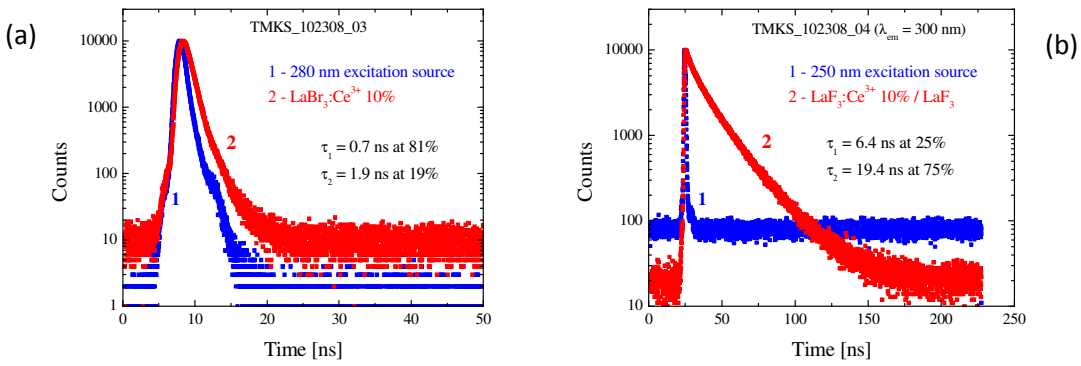

Figure 7.6: PL lifetime measurement plots of (a) anhydrously synthesized cerium-doped lanthanum bromide core colloidal NCs and (b) anhydrously synthesized cerium-doped lanthanum bromide/undoped lanthanum fluoride colloidal NCs

The cerium-doped lanthanum bromide core NCs show a very fast PL decay time of 0.7 ns (81%) and 1.9 ns (19%), as shown in Figure 7.6(a). The sub-nanosecond component was suspected to be arising from the excitation source decay due to the proximity of the excitation (280 nm) and the observation position on the PL emission spectrum (316 nm).

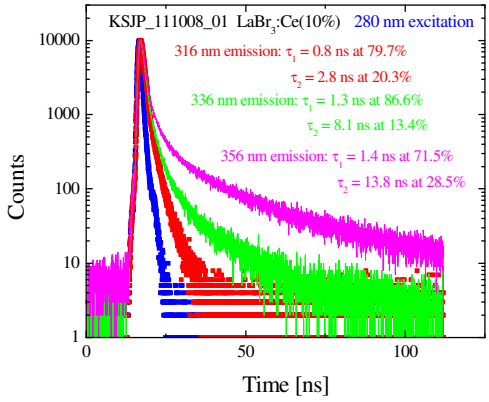

Figure 7.7: Shorter lifetime component diminishes as the lifetime is measured farther away from the excitation

In order to verify this, lifetime was measured at different points on the spectrum on the higher wavelength side of the PL emission peak. As observed in Figure 7.7, the weight of the longer lifetime component increases as the observation wavelength moves away from the excitation wavelength. This verifies the notion that the shorter component should be attributed to the excitation source. The core/shell NCs show an increased but still fairly short lifetime of 19.4 ns (75%) and 6.4 ns (25%), as shown in Figure 7.6(b).

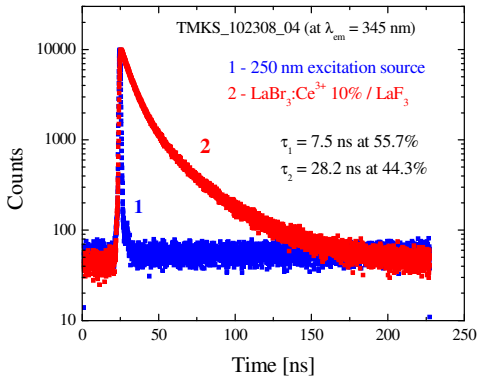

Figure 7.8: The shorter lifetime component is more pronounced at the shoulder (345 nm)

However, the lifetime measured at the shoulder at 345 nm showed a considerable increase in the shorter lifetime component, as shown in Figure 7.8, which can be tentatively associated with surface/defect related transitions.

7.5. Summary

The TEM, EDS, and PL results confirm that the novel anhydrous synthesis of the cerium-doped lanthanum bromide core colloidal NCs was successful. The corresponding anhydrously synthesized cerium-doped lanthanum bromide/undoped lanthanum fluoride core/shell colloidal NCs showed larger size in TEM images, an increased and blue-

shifted PL intensity, and a longer PL lifetime, hence that synthesis is also deemed successful. The increased PL intensity and lifetimes are expected due to the separation of the active luminesce centers from the emission quenching hydroxyl groups by the shell, whereas the blue-shift is possibly attributed to the compressive strain on the active core region of the nanocrystals.

References

1. Gao, D., and M. Michael. “Electronic structure study of cerium doped scintillators” *APS Meeting,* March (2008).

2. Kruk, D., O. Lips, P. Gumann, A. Privalov, and F. Fujara. “Dynamics of fluorine ions in LaF_3-type crystals investigated by NMR lineshape analysis” *J. Phys.:condens. Matter* 18, no. 17 (2006): 25-41.

3. Liu, B., M. Gu, Z. Qi, X.O. L. Liu, S. M. Huang, and C. Ni. “First-priciples study of lattice dynamics and thermodynamic properties of $LaCl_3$ and $LaBr_3$” *Physical Review B* 76, no. 6 (2007) Art.: 4307: 1-7.

4. Shah, K. S., J. Glodo, M. Klugerman, W. W. Moses, S. E. Derenzo, and M. J. Weber. “$LaBr_3$:Ce scintillators for gamma-ray spectroscopy” *IEEE Transactions on Nuclear Science* 50, no. 6 (2003): 2410-2413.

5. van Veggel, F. C. J. M., and J. W. Stouwdam. "Improvement in the luminescence properties and processability of LaF_3/Ln and $LaPO_4$/Ln nanoparticles by surface modification" *Langmuir* 20, no. 26 (2004): 11763-11771.

6. Wang, Z., J. Bo, S. Song, L. Hu, J. Liu, and X. Zhen. "One-step synthesis of highly water-soluble LaF_3:Ln^{3+} nanocrystals in methanol without using any ligands" *Nanotechnology* 18, no. 46 (2007): 465-476.

Chapter 8

Conclusions and future work

8.1. Conclusions

Cerium-doped lanthanum fluoride nanocrystals have been synthesized successfully through two different synthesis routes, their optical characteristics confirmed by absorption, PL excitation, and emission spectroscopy, and their structural and compositional characteristics determined through transmission electron microscopy and electron dispersive spectroscopy, respectively. These nanocrystals can be lucratively used as highly efficient size independent down-conversion biological markers, and as scintillation detectors for high-energy ionizing radiation spectroscopy. The characteristics of cerium-doped lanthanum halide bulk crystal systems have been studied extensively (Moses and Derenzo 1990), (Wojtowicz *et al.* 1994). Inorganic nanocrystals have been found to be advantageous for various applications (Parak *et al.* 2003), (Chen and Belbot 2005). Cerium-doped lanthanum bromide has been identified as a unique system that can provide fast (25 ns) emission at the short-UV wavelengths along with other key properties necessary for realizing high-efficiency scintillation detectors, such as high light yield, and high energy resolution for high-energy 662 keV gamma rays (Kramer *et al.* 2006), (Stouwdam and van Veggel 2002). However, the crystals suffered from severe limitations such as high cost, fragility, and the highly hygroscopic property. To overcome these limitations, core/shell structure of cerium-doped lanthanum bromide/stable lanthanum fluoride was synthesized through facile and inexpensive colloidal routes. As the first step in the systematic approach, core and core/shell NCs of cerium-doped

lanthanum fluoride were synthesized using the water-based (aqueous) and water-free (anhydrous) synthesis routes, among which the latter was developed indigenously. From the characterization results of cerium-doped lanthanum fluoride NCs, the signature intra-configurational cerium-ion emission characteristics could be verified using 250 nm UV excitation of the internal cerium levels.

Using the indigenously developed anhydrous synthesis route in methanol, cerium-doped lanthanum fluoride/undoped lanthanum fluoride core/shell NCs were synthesized successfully as indicated by structural and optical characterization results.

Furthermore, 10% cerium concentration was empirically identified as the optimum cerium concentration (x) in the $Ce_xLa_{1-x}F_3$ NC system in terms of light output from the activator levels of cerium. The results were repeatable, since they were independent of the synthesis route. It has been inferred from the analysis of bulk crystals that the emission starts decreasing at cerium concentrations higher than 10% due to the increased presence of perturbed cerium ions that compete with the activator emission channel (Wojtowicz *et al.* 1994).

The persistence to high energy ionizing radiation was tested with a monoenergetic ^{137}Cs 662 keV gamma source. Cerium-doped lanthanum fluoride NCs were tested in comparison with CdSe/ZnS NCs. The former showed excellent radiation hardness with only 20% reduction in PL light output after extensive exposure to gamma radiation (2400 krads) whereas the latter lost almost 50% of light output after just 11.5 krads of gamma exposure. A reduction in PL lifetime was also observed with the irradiated sample, which may be due to creation of nonradiative recombination centers in the material.

Finally, following this systematic approach, cerium-doped lanthanum bromide core NCs were synthesized anhydrously in methanol, though due to the sample's hygroscopic nature, it had to be stored and handled hermetically. The TEM images provided evidence for good crystallinity of the nanocrystals and EDS confirmed the elemental composition.

The idea of coating the hygroscopic NCs with the stable lanthanum fluoride shell to form stable core/shell NCs was successful. The spectral shift is tentatively interpreted as the effect of compressive strain on the active core due to difference in lattice constants between core and shell crystals. In conclusion, the systematic approach with the development of indigenous anhydrous synthesis method lead to the first ever synthesis of cerium-doped lanthanum bromide with stable lanthanum fluoride shell as colloidal nanocrystals.

8.2. Future work

This thesis work presents the first step or the initiative taken in identifying the right material for a long term goal of designing a portable, low-cost, and high-performance gamma ray scintillation detector, thereby providing ample scope for future work. A terse description of the proposed scintillation detector system is provided in Figure 8.1.

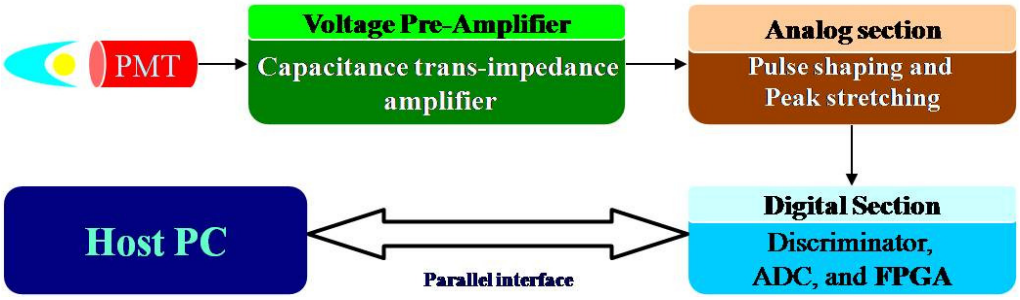

Figure 8.1: Basic schematic of the proposed pulse-height analysis system for cerium-doped lanthanum-halide-based scintillation detection system

Two events are possible when gamma radiation encounters a scintillating material: photo-electric photon to electron conversion and/or Compton scattering. The electrons excited as a result of photo-electric effect relax back, emitting photons characteristic to the material. As a result, the response curve of the scintillator shows photo-electric peaks superimposed over a continuous Compton background. The absolute pulse height of the photo-peaks corresponds to the energy of the gamma radiation. Then, the photodetector will convert the photo-peaks into current pulses which will be sufficiently amplified into voltage signal by the pre-amplifier. The mV signal obtained from the pre-amplifier will be amplified to a linear range of 0-10V using an inverting amplifier along with a pole/zero compensation network and an offset adjustment circuit. Subsequently, the pulse-shaping circuit will generate a semi-gaussian pulse of the same height as the incoming pulse to satisfy the shape requirements of the following electronics. The signal from the gain stage will be fed both to a fast-shaping (30 ns) second-order inverting low-pass filter and a cascade of two non-inverting low-pass filters (150 ns) with a gain higher than the one in the middle frequency range. The fast-shaping filter will be used to detect more than one peak occurring in the sampling time interval (pile-up rejection). The peak stretching circuit will then stretch the semi-gaussian peak to nearly a square wave, which is required to compare steady voltage levels with reference voltage for pulse height analysis. The discriminator will allow only the signals above a certain threshold to be sent to the analog to digital convertor (ADC). This improves signal-to-noise ratio. The ADC will help converts the flat peak voltage level normalized between 0-10 V into a 12-bit data word. The FPGA will perform functions such as data acquisition, issuing trigger and reset signals, pile-up removal logic, read/write to on-chip block RAM, and

input/output interfacing. The output will be a histogram of pulse heights corresponding to detected gamma radiation energies spread over a range of channels. The basic skeleton of this system is usually called a multi-channel analyzer (MCA) that is used extensively for pulse-height analysis in radiation detection field. Here, it is proposed to use a customized MCA that can be tuned to be specific to the material system.

Further scope exists for better understanding of the newly synthesized cerium-doped lanthanum bromide/undoped lanthanum fluoride core/shell nanocrystals. This includes optimization of Ce content in $LaBr_3$ NCs for maximum quantum efficiency, optimization of LaF_3 shell thickness for best protection of $LaBr_3$ core without introducing defects due to excessive strain, demonstration of scintillation of $LaBr_3$:Ce/LaF_3 NCs under gamma irradiation, and determination of optimal host material for $LaBr_3$:Ce/LaF_3 nanoscintillators. This concludes this thesis work.

References

1. Chen, G. Y., and M. Belbot. "Improving energy resolution of scintillation detectors" IEEE *Nuclear Science Symposium* (2005): 235-238.
2. Kramer, K. W., P. Dorenbos, H. U. Gudel, and C. W. E. van Eijk. "Development and characterization of highly efficient new cerium-doped rare earth halide scintillator materials" *Journal of Materials Chemistry* (2006): 2773-2780.
3. Locock, A., and P. Burns. "The crystal structure of synthetic autunite, $Ca[(UO_2)(PO_4)]_2$ $(H_20)_{11}$" *Am. Mineral.* 88 (2003): 240-244.

4. Moses, W. W., and S. E. Derenzo. "The scintillation properties of cerium-doped lanthanum fluoride" *Nuclear Instruments and Methods in Physics Research* A 299 (1990): 51-56.
5. Parak, W. J., D. Gerion, T. Pellegrino. "Biological applications of colloidal nanocrystals" *Nanotechnology* 14, no. 2 (2003): 1123-1137.
6. Stouwdam, J. W., and F. C. J. M. van Veggel. "Near-infrared emission of redispersible Er^{3+}, Nd^{3+}, and Ho^{3+} doped LaF_3 nanoparticles" *Nano Letters* 2, no. 7 (2002): 733-737.
7. Wojtowicz, A. J., M. Balcerzyk, E. Berman, and A. Lempicki. "Optical spectroscopy and scintillation mechanisms of $Ce_xLa_{1-x}F_3$" *Phys. Rev. B* 49, no. 21 (1994): 880-892.